

ALPHA FOUNDATION FOR THE IMPROVEMENT OF MINE SAFETY AND HEALTH

Final Technical Report

Project Title: Validation of the Gas and Dust Explosion Model

Grant Number: AFSTI14FO-82

Organization: West Virginia University (WVU)

Principal Investigator: V'yacheslav (Slava) Akkerman

Contact Information : 1306 Evansdale Drive, Morgantown, WV 26506-6106

Email: Vyacheslav.Akkerman@mail.wvu.edu

Phone: 304-293-0802 **Fax:** 304-293-6682

Period of Performance: January 1st, 2019 – June 30th, 2020 (18 months)

Acknowledgement/Disclaimer: This study was sponsored by the Alpha Foundation for the Improvement of Mine Safety and Health, Inc. (ALPHA FOUNDATION). The views, opinions and recommendations expressed herein are solely those of the authors and do not imply any endorsement by the ALPHA FOUNDATION, its Directors and staff.

1.0 EXECUTIVE SUMMARY

Historically, accidental gas and dust explosions constitute one of the major hazards to both personnel and equipment in industries dealing with explosive materials, with primary application in coalmining industry. Since existing knowledgebase on such explosions did not provide an acceptable level of risk, novel preventive mining/fire safety strategies, based on a rigorous predictive scenario for explosion developments were critically needed. This constituted the motivation, objective and overall content of this project: further improvement and *validation* of the Gas & Dust Explosion Model – an integrated analytical, computational and experimental platform providing a predictive/descriptive coalmining fire scenario focusing on flame/pressure evolutions in explosions occurring in obstructed enclosures.

The experimental component of this project comprised a series of experiments on explosion venting. Specifically, the influence of the vent area on the overpressure and dynamics of lean, stoichiometric, and rich methane-air flames is studied. The experimental parametric study included ignition location, central or rear, and three various vent areas (with negligible vent relief pressure). As expected, the highest maximum pressure was associated with the stoichiometric conditions and the smallest vent area. For a fuel-rich mixture with central ignition, a flashback phenomenon was observed after an external explosion. The experimental study was subsequently extended to a twice longer cylinder with and without a secondary compartment. An engineering model predicting the pressure evolution in methane-air vented deflagrations was updated and compared to the experiments, with agreement between the experiments and the simulations in terms of pressure rise and peak pressures observed.

Within the theoretical component of this project, the theory for a globally-spherical, self-accelerating expanding premixed flame front was combined with that of extremely fast flame acceleration in obstructed conduits to form a new analytical formulation. The coalmining geometry is imitated by long passages of high aspect ratio, with a comb-shaped array of tightly-placed obstacles attached to the walls. Specifically, the key stages of premixed flame front evolution are identified and scrutinized, by quantifying their major characteristics such as the flame tip position and its velocity. Starting with an incompressible assumption, the analysis has been subsequently extended to account for gas compressibility, because the latter cannot be ignored as soon as the flame velocity starts approaching the speed of sound. It was shown that the effect of gas compressibility moderates flame acceleration, and such an impact depends strongly on various thermal-chemical properties of the combustible mixture. The theoretical investigation of the problem revealed that the influence of both the obstacles and the combustion instability on the fire scenario was substantial, and this effect grew stronger with the blockage ratio. Starting with gaseous methane-air combustion, the formulation was subsequently extended to gaseous-dusty environments. Specifically, the coal (combustible, i.e. facilitating the fire) and inert (such as sand, moderating the process) dust and their combinations were considered. The impact of the size and concentration of the dust particles on flame acceleration has been quantified.

The computational component of the project includes two different computational platforms – one is a comprehensive CFD-based solver D-GEM, adopted for parallel, multi-phase computations, while the other is a simplified, zero-dimensional mathematical explosion vent analyzer (EVA). Both platforms have been developed (in part, at least) and upgraded due to the support from the Alpha Foundation.

Finally, the analytical predictive scenario has been compared to the experiments and the numerical simulations – from the literature, as well as in-situ experiments and modelling performed within the frame of this project, with good agreement obtained. Likewise, the present experimental work agrees with the EVA modelling. Consequently, a newly-developed integrated analytical, computational and experimental Gas & Dust Explosion Model has been validated within the range of its applicability.

2.0 PROBLEM STATEMENT AND OBJECTIVE

The ultimate goal of the present project, ASTI14FO-82, which is an extension of the previous Alpha Foundation's project ASTI14-05, has been further development, extension and validation of the joint experimental, analytical and computational platform – to be able to predict and quantify the mining fire hazards such as the probability of spontaneous ignition, the evolution of a fire flame front if occurred, and likelihood of the deflagration-to-detonation transition if relevant.

Within such an integrated platform, the objective of the analytical component of the project was to be able to predict, quantitatively, the entire scenario of premixed flame front evolution within an accidental fire, with the situation of a methane-air explosion in a mining passage as the primary application. Specifically, the key stages of the flame evolution have been scrutinized for various flame acceleration mechanisms, and it was aimed to identify the key characteristics of all these stages such as the timing for each stage as well as the flame shapes, propagation speeds, acceleration rates, run-up distance and flame-generated velocity profiles. Both gaseous and gaseous-dusty (which is more practical) mining environments have been targeted, and in the latter case, both inert and combustible dusts were considered. The thermal-chemical parameters of particle-air flames have been tabulated as functions of the particle type, size and concentration by means of the *Seshadri* formulation, which will be summarized below. For the validation purpose, the analytical component was aimed to be supported by the in-situ experimental endeavors at Worcester Polytechnic Institute (WPI) as well as by comprehensive computational simulations of two types.

First, we have aimed to further develop a CFD-based computational platform entitled Dust and Gas Explosion Model (D-GEM). Having a fully-compressible, finite-volume Navier-Stokes code solving for the set of hydrodynamics and combustion equations in homogeneously-gaseous laminar environment as a core of the newly-being-developed platform, the D-GEM was aimed to be extended to gaseous-dusty environments by incorporating the combustible and inert dust particles into the D-GEM via the thermal-chemical parameters of particle-air flames (again, tabulated as functions of the particle type, size and concentration by means of the *Seshadri* formulation).

A separate, second component of the computational efforts was aimed to further develop and extend another computational model – the mathematical explosion venting analyzer (EVA) – a simplified zero-dimensional code solving for the corresponding basic equations in a one-zone approximation, including the external explosion produced once the vented mixture is ignited by the expanding flame, to compute the attained overpressure in relation to the domain geometry and combustion conditions.

Briefly speaking, the general idea of the classical *Seshadri* formulation is the following: while the CFD modelling of multiphase systems (such as fluids with solid dust) is typically difficult (especially if such systems are chemically-reacting), if a fraction of a solid phase is less than a certain threshold, we replace such a multiphase system by an "*effective fluid*", which properties (transport coefficients, laminar flame velocity etc.) are modified ("*dust-induced*"). So, with this adjustment, we deal with one phase, which certainly makes our consideration easier as compared to a detailed multi-phase study.

This is a clear advantage of the *Seshadri* model, so we incorporated it both into the CFD platform and into the analytical formulation. In the future, it will be also interesting to incorporate it into the EVA.

While a pilot version of such an integrated analytical-computational-experimental platform has been developed within the frame of the previous project, ASTI14-05, the outcomes of this research were "academic" to some extent such that a set of parameters from real coalmines remained unknown. Consequently, there was a need to quantify these unknown parameters and new features, such as in-built obstacles, and then provide a more robust validation of the model to justify its applicability to capture combustion in coalmines. As a result, there was a critical need to reduce the gap between the academic study and practical applications by validating the D-GEM, the EVA and the analytical model.

While some validation has been done within the initial project, ASTI14-05, a more robust validation of the model has been required and desired before proceeding further with its development or assessment of specific applications. Consequently, the ways to provide such a successful validation constituted the motivation, objectives and overall content of the present project. To be specific:

- First, we aimed to perform in-situ experiments at WPI to validate our model. WPI's Professor Ali S. Rangwala has been a subcontractor overseeing the entire experimental work.
- Second, it has been highly important to compare our model to the available research outcomes of other researches working in the field of coalmining fire safety. In this respect, we aimed to pay a special attention to the comprehensive numerical simulations conducted at the University of Maryland (UMD), College Park, within Alpha Foundation's project AFC215-20. Specifically, we aimed to validate our model by comparing with the numerical simulations AFC215-20 for a wide range of thermal-chemical parameters, with similarities and differences aimed to be identified.
- To the best of our knowledge, the main difference between our computational approach and that of the UMD project AFC215-20 is that we have incorporated the Seshadri model, thereby reducing the complexity. Moreover, the present project includes a separate analytical formulation, which it is actually the major item of our work.
- A special attention has been aimed to be paid to extend the theoretical approach from one based on finger flame acceleration to that based on obstacles. Indeed, while obstacles appeared beyond our analysis in the previous project, ASTI14-05, we subsequently recognized the importance to account for obstacles in a coalmine fire scenario because coalmines usually involve long tunnels with possible crosscuts and with rubble or equipment on the floor, constituting blockages.
- Consequently, it has been aimed to combine the mechanisms of flame acceleration in tunnels, due to (i) finger-like flame shape, (ii) wall friction, and (iii) obstacles faced on the flame track, into a unified analytical approach. It has been aimed to start the analysis with laminar homogeneously-gaseous combustion and then extend it to the dusty-gaseous environments.
- It was also aimed to perform an extensive literature overview in order to secure the relevant data available in literature, and to validate the newly-developed model by such a data, when possible.

3.0 RESEARCH APPROACH

The overall integrative research approach consists of four (4) distinguished components, specifically: (i) the experiments performed at WPI; the two numerical platforms, namely, (ii) the computational fluid dynamics (CFD) solver (GEM/D-GEM) as well as (iii) the computational Explosion Vent Analyzer (EVA); and (iv) the analytical component. All of them are detailed below, respectively, in Secs. 3.1, 3.2 and 3.3. Among these components, the analytical part is a major stand-alone solution element, but in order to make an overall approach integrative, we performed multiple validations, by comparing our theory, modelling and experiments to each other (when applicable) as well as to the modelling and experiments available in the literature.

3.1 Experimental Approach

3.1.1 One-compartment setup – Description. Figure 1 is a schematic of the original experimental setup, developed at the Worcester Polytechnic Institute (WPI), while the side and the front photos of this setup are presented in Fig. 2. Namely, a cylindrical vessel of length 30 cm and diameter 9 cm is used such that the aspect ratio is ~ 1.5 , and the volume of this cylinder is circa 8,5000 cm³. The center ignition is considered, with the circular vent areas

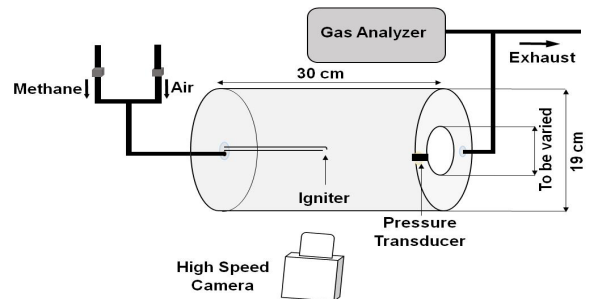


Fig. 1: A sketch of one-compartment experimental setup: the front panel accommodates the vent while the rear panel is used for gas injection and probes.

of diameters from 8 cm till 13 cm. The experiments are video-recorded to visualize flame propagation inside the vessel and its impact on the explosion overpressure. For optical access, the transparent vessel is made of polycarbonate. To be unmoved, it is attached to a steel bench with C-clamps. The circular vents are arranged at one side of the cylinder, with the vent areas $A_v = 67.9, 86.6,$ and 132.7 cm^2 . For the initial sealing, the vents are covered with a thin aluminum foil of thickness 0.03 mm. Prior to ignition, the center of the foil is cut in the horizontal and vertical directions to provide a free-venting condition as shown in Fig. 2b.

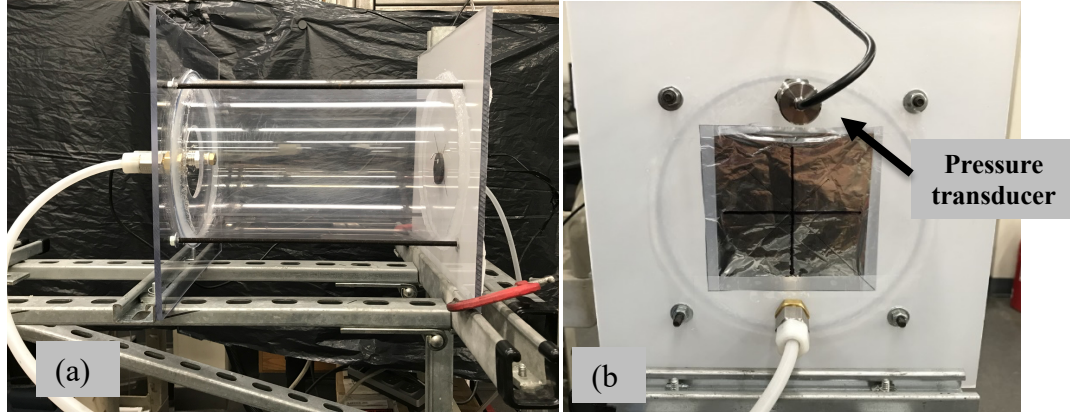


Fig. 2: The side (a) and front (b) views of the cylinder. The plus shape marked on the foil shows the cut.

The chamber was initially filled with air. Then, methane (CH_4) and air are supplied using the mass flow controllers. In all experiments, a natural injection of the CH_4 and air gases into the cylinder was conducted imitating the conditions of methane accumulation inside a coalmining passage. First, a slightly excessive amount of methane was injected into the chamber from the rear center of the cylinder, with a preset mass flow rate. Subsequently, additional small amounts of air have been supplied into the chamber to bring the mixture composition to the test condition and to flush the methane gases inside the inlet hose. A gas analyzer is employed to monitor the composition of the methane-air mixture inside the vessel, and the steady readings from the gas analyzer were obtained for the test conditions prior to ignition. Ignition is triggered by a 1.5 V spark igniter located at the center or side of the vessel.

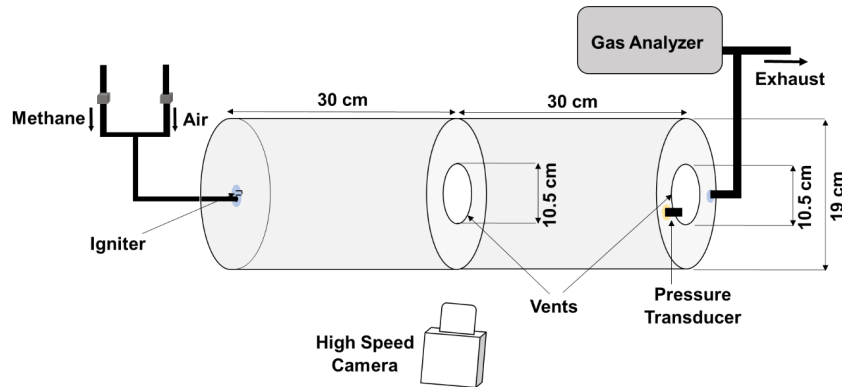


Fig. 3: The two-compartment experimental setup.

3.1.2 Two-compartment setup - Description. The cylindrical vessel was subsequently extended twice and splat into two equal compartments. Consequently, instead of a one-compartment setup of Fig. 1, the two-compartment vessel was 60 cm in length and had two vents of a similar size as sketched in Fig. 3. The diameter of the cylinders in all the setups was 19 cm. The experiments at three equivalence

ratios ($\phi = 0.8; 1; 1.2$) were carried out three times and the results showed good repeatability. Each chamber was initially filled with the ambient air. Then, the methane and the air were supplied to the vessel using the mass flow controllers. First, methane (in the amount slightly higher than that needed for the test condition) was injected into the chamber from the rear center of the cylinder. Then, the proper amount of air needed to bring the mixture composition to the test condition was injected.

3.1.3 Experimental methodology. Evolutions of overpressure, the flame tip position and velocity, the burnt gas volume, the flame front surface area as well as the flame overshoot (the length of the flame after venting) have been recorded. Overpressure is measured by a pressure transducer, with the data captured every millisecond. The flame images inside and outside the vessel are recorded by a high-speed camera, with a rate of 1,057 frames/sec. Overall, each experiment was repeated no less than three times, with good repeatability.

The Matlab and ImageJ are used to post-process the images obtained in the experiments, with a Matlab code employed to calculate the flame tip position, velocity, and acceleration rate as well as the external flame length, while the ImageJ software is used to modify the images as needed. Figure 3 illustrates the ImageJ processing. Specifically, to achieve accuracy/high-quality of the flame images, the following processes were employed: (i-ii) an image is converted into a gray scale; (iii) a Sobel edge detector is used to highlight sharp edges/gradients; (iv) the background and foreground colors are switched to bring the flame to the foreground; (v) the degrees of brightness and contrast are adjusted to reveal the flame front with better resolution; and, finally, (vi) noises are removed.

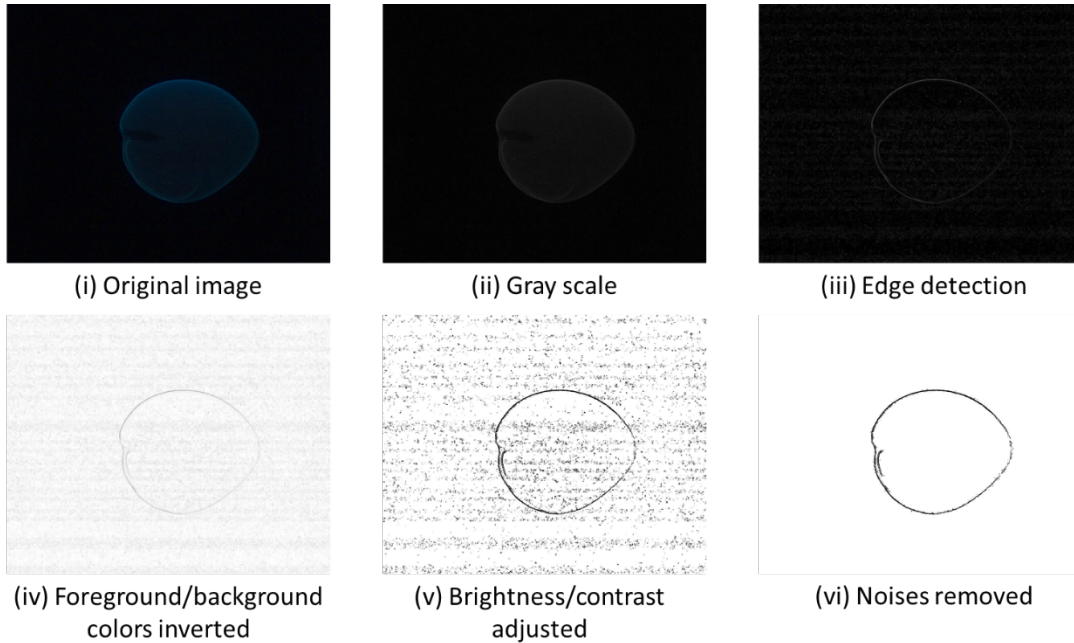


Fig. 4: The image analysis of the video frames.

3.2 Computational Approaches

Two different computational platforms (developed, partly, with the support of the Alpha Foundation) have been developed, extended and employed in this project. As detailed bellow, one of them is the comprehensive CFD solver entitled GEM/D-GEM, while the other is the simplified zero-dimensional computational Explosion Vent Analyzer (EVA). It is recalled that the originality of our CFD approach (as compared to other concomitant studies such as the UMD project AFC215-20) is, in particular, that we have incorporated the Seshadri model, thereby reducing the complexity of a multi-phase problem.

3.2.1 GEM/D-GEM model description. In the previous project Alpha Foundaiton's project ASTI14-05 we initiated the development of the computational dust and gas explosion model (GEM/D-GEM), which is based on the first principles of hydrodynamics and combustion. Such a platform does not involve any empirical correlation and therefore it should potentially work everywhere within its validity domain, without addiction to any particular experiment/configuration. The backbone of the platform is a robust "in-house" Navier-Stokes code, which solves fully-compressible hydrodynamics and combustion equations. The numerical scheme is 2nd-order accurate in time and 4th-order in space for the convective terms, and 2nd-order in space for the diffusive terms. The platform uses self-adaptive structured computational grid, which makes it suitable to simulate the domains with large aspect ratio such as mine tunnels. The solver is available in the two-dimensional (Cartesian and cylindrical axisymmetric) versions as well as in the three-dimensional Cartesian version. This platform is adapted for parallel computations. It is noted that the very embryo of the platform was developed originally at Volvo Aero, and it has subsequently been updated, comprehensively, by several research groups in Sweden and the U.S. This embryonic core of the platform has been justified by successful employment towards modeling of various practical aero-acoustic and combustion applications. Some description of this embryo of the platform is available, in particular, in Ref. [1]. The governing equations read:

$$\frac{\partial \rho}{\partial t} + \frac{\partial}{\partial x_i}(\rho u_i) = 0, \quad (3.1)$$

$$\frac{\partial}{\partial t}(\rho u_i) + \frac{\partial}{\partial x_j}(\rho u_i u_j + p \delta_{ij} - \gamma_{ij}) = 0, \quad (3.2)$$

$$\frac{\partial}{\partial t}\left(\rho \varepsilon + \frac{1}{2} \rho u_i u_i\right) + \frac{\partial}{\partial x_j}\left(\rho u_j h + \frac{1}{2} \rho u_i u_i u_j + q_j - u_i \gamma_{ij}\right) = 0, \quad (3.3)$$

$$\frac{\partial}{\partial t}(\rho Y) + \frac{\partial}{\partial x_i}\left(\rho u_i Y - \frac{\mu}{Sc} \frac{\partial Y}{\partial x_i}\right) = -\frac{\rho Y}{\tau_R} \exp(-E_a/R_u T), \quad (3.4)$$

respectively, where Y is the mass fraction of the fuel mixture, $\varepsilon = QY + C_v T$ is the specific internal energy, $h = QY + C_p T$ is the specific enthalpy, Q is the energy release in the reaction, C_v and C_p are the specific heats at constant volume and pressure, respectively. Equation (3.4) employs a one-step irreversible Arrhenius reaction of the first order, with the activation energy E_a and the constant of time dimension τ_R . Finally, the stress tensor γ_{ij} and the energy diffusion vector q_j are given by

$$\gamma_{ij} = \zeta \left(\frac{\partial u_i}{\partial x_j} + \frac{\partial u_j}{\partial x_i} - \frac{2}{3} \frac{\partial u_k}{\partial x_k} \delta_{ij} \right), \quad (3.5)$$

$$q_j = -\zeta \left(\frac{C_p}{Pr} \frac{\partial T}{\partial x_j} + \frac{Q}{Sc} \frac{\partial Y}{\partial x_j} \right), \quad (3.6)$$

where ζ is the dynamic viscosity. The combustible mixture conventionally consists of a diatomic perfect gas of a constant molecular weight $m = 2.9 \times 10^{-2}$ kg/mol, with $C_v = 5R_u/2m$, $C_p = 7R_u/2m$, where $R_u = 8.314$ J/(mol K) is the universal gas constant, and the equation of state is $P = \rho R_u T/m$. Combustion is characterized by the planar flame speed S_L and the flame thickness L_f . While the system (3.1)-(3.4) generally describes a homogenous fluid, we next implemented dust particles by modifying the Seshadri formulation [2] for the flame speed $S_L \rightarrow S_{L,d}$:

$$S_{L,d} = \frac{1}{Ze} \sqrt{\frac{2Bk_u}{\rho_u C_T} \exp\left(-\frac{E_a}{R_u T_f}\right)}, \quad Ze = \frac{E_a(T_f - T_u)}{R_u T_f^2}, \quad (3.7)$$

where Ze is the Zeldovich number, and C_T is the total heat capacity of the mixture, which includes the dust term inside, and can be calculated as

$$C_T = C_p + C_s \frac{4\pi r_s^3}{3} \frac{\rho_s}{\rho} n_s, \quad (3.8)$$

where C_p is the heat capacity of the gas phase, C_s is the heat capacity of particles and ρ is the density of the mixture, expressed as $\rho = \rho_u + c_s$, where ρ_u is the gas density, c_s is the concentration of the particles, and $n_s = (c_s / \rho_s) / V_s = 3(c_s / \rho_s) / 4\pi r_s^3$ is the amount of dust particles per unit volume.

3.2.3 EVA model description. The mathematical model upgraded and employed in this project – the Explosion Vent Analyzer (EVA) – has been developed by Ugarte *et al.* [3], and it underwent several modifications [4]. The EVA is a transient, reduced-order (zero-dimensional; 0D) model used to predict the maximum (over)pressure, the mass transfer, and the flame speed during explosions in vented and unvented enclosures. The EVA is capable to estimate the explosion characteristics in various geometries by solving the mass and energy balance equations, and the combustion rate formulations.

The mass balance:

$$\frac{d}{dt} \left(\frac{m_u}{m_i} \right) + \frac{d}{dt} (n) + \frac{d}{dt} \left(\frac{m_v}{m_i} \right) = 0, \quad (3.9)$$

$$\frac{m_u}{m_i} = \frac{1}{\bar{P}\gamma_u} (1 - \bar{V}), \quad n = \frac{m_b}{m_i}. \quad (3.10)$$

Here, t and m stand for the time and mass, respectively, the subscripts u, b, v , and i designate the unburned, burned, vented, and initial conditions, $\bar{P} = P/P_i$ is instantaneous-to-initial pressures ratio, \bar{V} is the initial volume occupied by the burnt gas, and $\gamma_u = C_p/C_v$ represents the specific heat ratio of the unburnt gas, employed from the NASA-CEA solver [5] embedded in the EVA to calculate the thermal-physical properties of the respective fuel-air mixtures.

The combustion rate formulation:

$$\frac{dn}{dt} = \frac{A}{V_i} S_T \bar{P}^{1/\gamma_u} - K \frac{d}{dt} \left(\frac{m_v}{m_i} \right). \quad (3.11)$$

Equation (3.11) determines the rate at which the burnt matter is generated, as a function of the combustion velocity with respect to the fuel mixture denoted as S_T , the surface area of the flame front A , and the initial volume of the fuel mixture denoted as V_i . The term K in Eq. (3.11) is used to specify the type of gas vented, with $K = 0$ if the unburned gas is vented, and $K = 1$ if the burnt gas is vented.

The energy balance:

$$\frac{d}{dt} [\bar{P}(1 - \bar{V})] + \frac{\gamma_u - 1}{\gamma_b - 1} \frac{d}{dt} (\bar{P}\bar{V}) = b \frac{dn}{dt} - \bar{P}^{(1-\frac{1}{\gamma_u})} \frac{d}{dt} \left(\frac{m_v}{m_i} \right), \quad (3.12)$$

$$b = (e_{uo} - e_{bo} + T_0 [C_{v_b} - C_{v_u}]) / C_{v_u} T_i, \quad \bar{V} = V_b / V_i. \quad (3.13)$$

Here, e_o is specific energy of formation, along with the reference temperature T_0 , the specific heat at constant volume C_v , and the specific heat ratio of the burnt gas γ_b . Further details of the original EVA model are given in Refs. [3,4].

3.2.4 EVA models for the flame shape. The flame shape is one of the major parameters imposed into the EVA solver, being either spherical or ellipsoidal. The latter is one of the modifications made to the original EVA platform. It is noted that the pioneering Mulpuru–Wilkin predictive explosion model [6] considered a spherical flame shape. Such a choice was suitable to predict the explosion dynamics in the configuration used in the experimental work, as there was good match between the experimental work and the model. However, for most geometries, the spherical flame assumption is not accurate,

leading to a notable discrepancy between the results of the predictive explosion model as compared to the experimental results.

According to Ref. [7] the flame shape influences the maximum peak pressure values as well as the explosion behavior. In particular, the ellipsoidal shape of the flame front in Ref. [7] provided better predictions of the explosion characteristics in the cylindrical geometry as compared to the spherical flame shape. Therefore, in the present work, where a cylindrical geometry is being considered, the ellipsoidal flame shape, illustrated in Fig. 5, is used. The fuel-air mixture for this work was ignited at the rear end far away from the vent area. Figure 5b therefore depicts the flame shape behavior better.

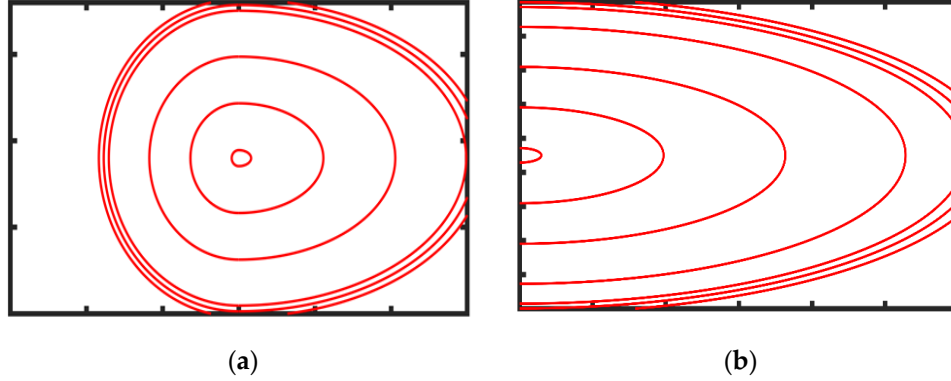


Fig. 5: The ellipsoidal flame geometry for (a) central ignition (CI) and (b) rear ignition (RI) [7].

3.2.5 EVA calculation of the flame speed. The laminar flame velocity S_L is a key parameter for predictive models characterizing explosions. Consequently, accurate determination of the value S_L yields a substantial effect on the accuracy of the results of the predictive model. When a particular S_L -value is not available, it is computed in the EVA by using the correlation formula [4,8]

$$S_L = S_{L,0} \left(\frac{T_u}{T_{u,0}} \right)^\alpha \left(\frac{P_u}{P_{u,0}} \right)^\beta \quad (3.14)$$

as a function of unburnt gas temperature, T_u , and pressure, P_u , scaled by their initial values $T_{u,0}$ and $P_{u,0}$. Here $S_{L,0}$ is the unstretched laminar flame velocity at the initial temperature and pressure, $S_{L,0} = S_L(T_{u,0}, P_{u,0})$, while the exponents α and β are usually functions of the fuel-to-oxidizer equivalence ratio ϕ . Stone *et al.* [9] suggested the following relations for the methane-air mixtures:

$$\begin{aligned} S_{L,0} &= 37.6 + 15.1(\phi - 1) - 221(\phi - 1)^2 - 458(\phi - 1)^3 - 358(\phi - 1)^4, \\ \alpha &= 1.42 + 1.98(\phi - 1), \quad \beta = -0.314 + 608(\phi - 1). \end{aligned} \quad (3.15)$$

As a result, in the present work, we use Eqs. (3.14) and (3.15) to calculate S_L . Another way to calculate the flame velocity, used in earlier works [10,11], is to employ combustion modeling software such as Cantera – an open-source chemical kinetics software having various available chemical kinetics model, embedded into it, to compute S_L . Specifically, Cantera identifies the laminar flame velocity by modelling a one-dimensional (1D) freely propagating laminar premixed flame front. Then the laminar flame speed is calculated as [12,13]

$$S_L = \frac{d^2m}{dt^2} \frac{1}{\rho_u}, \quad (3.16)$$

where ρ_u is the density of the unburnt gas, while the quantity d^2m/dt^2 for the mass flux through a freely propagating flame is calculated according to Ref. [14]. Further details regarding how Cantera

calculates the flame speed for various fuel-oxidizer mixtures can be found in Refs. [12-14]. It is also noted that local variations of S_L may influence propagation and morphology of a global flame front, and such an impact can be either supportive or preventive, as we have recently showed in Ref. [15].

Finally, it should be mentioned in passing that, originally, the EVA appeared as a "side" product of our projects, but the more we deal with the EVA, the more we appreciate its appearance. Indeed, being much faster and easier to use than the CFD tools, it sometimes shows comparable (or not much worse) results. It is also noted that the EVA can be used in the case of *no venting* - we simply employ the vent area to be zero in that case. However, generally speaking, we prefer to use the EVA when other tools such as CFD solvers are not (or worse) applicable, for instance, in the case of venting. Furthermore, the EVA and the CFD tools usually investigate different parameters and features. For instance, the EVA is a zero-dimensional (0D) tool, which scrutinizes pressure (overpressure), while by means of CFD we typically consider the velocity fields and the flame velocity.

3.3 Analytical Approach

3.3.1 Development of a predictive scenario for a methane-air-dust fire in a coalmining passage. We considered a passage (channel) of width $2H = 2.1$ m as illustrated in Fig. 6, which is closed at one end and a premixed flame propagates towards the open end. The passage was blocked by obstacles of length αH such that channel along the central part $(1 - \alpha)H$ is unobstructed.

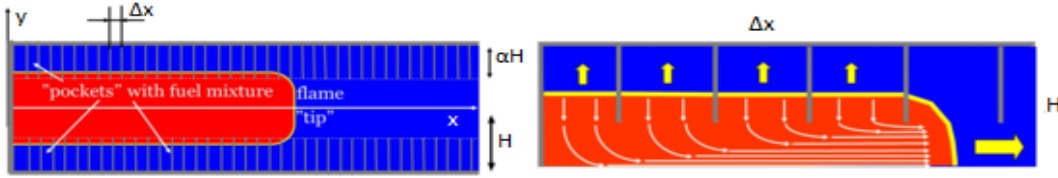


Fig. 6: An illustration of the Bychkov mechanism of flame acceleration in an obstructed passage [16].

From the ignition time and until a flame "skirt" contacts an obstacle at a time instant t_{obs} , the flame evolution is described by the predictive scenario of the explosion development in an *unobstructed* coalmining passage [17], which combines the mechanism of flame acceleration caused by a finger flame shape [18] with that of a globally-spherical, expanding flame front corrugated due to the Darrieus-Landau (DL) instability [19]. The global radius of an expanding flame corrugated by the DL instability obeys the power law, $R_f \propto t^n$, $n = 1.3 \sim 1.5$, so that instead of the unstretched laminar flame velocity U_f , the instantaneous radial flame velocity with respect to the fuel mixture is [19]

$$U_{DL}(t) = U_f \left(\frac{\Theta}{n} k_{DL} \right)^{n-1} t^{n-1}, \quad k_{DL} = L_f^{-1} \left\{ 1 + \frac{(\Theta - 1)}{(\Theta - 1)^2} \Theta \ln \Theta \right\}^{-1}, \quad (3.17)$$

where $\Theta \equiv \rho_{fuel}/\rho_{burnt}$ is the thermal expansion ratio, $k_{DL} \equiv 2\pi/\lambda_{DL}$ is the Darrieus-Landau cut-off wavenumber, and $L_f \equiv D_{th}/U_f$ is the flame thickness, with the fuel thermal diffusivity D_{th} . Demir *et al.* [17] combined the above analysis with the mechanisms of finger flame acceleration [18] into a unified formulation for a fire scenario in an unobstructed passage, with the evolution of the flame "skirt" position $R_f(t)$, the flame tip position $X_{tip,f}(t)$, and the flame tip velocity $U_{tip,f}(t)$ given by [17]:

$$R_f(t) = \frac{\Theta H}{\Theta - 1} \left\{ 1 - \exp \left[-\frac{\Theta - 1}{\Theta H} \left(k_{DL}^{n-1} \left(\frac{\Theta U_f}{n} \right)^n \right) t^n \right] \right\}, \quad X_{tip,f} = \frac{\Theta H}{\Theta - 1} \left\{ \exp \left[\frac{\Theta - 1}{\Theta} \frac{k_{DL}^{n-1}}{H} \left(\frac{\Theta U_f}{n} \right)^n t^n \right] - 1 \right\},$$

$$\frac{dX_{tip,f}}{dt} = U_{tip,f} = n k_{DL}^{n-1} \left(\frac{\Theta U_f}{n} \right)^n t^{n-1} \exp \left[\frac{\Theta - 1}{\Theta} \frac{k_{DL}^{n-1}}{H} \left(\frac{\Theta U_f}{n} \right)^n t^n \right]. \quad (3.18)$$

Similar to Ref. [17], we took $n = 1.4$ and the thermal chemical parameters of the combustible mixture [20]. In an unobstructed passage, the formulation (3.17) will work until the instant when the flame skirt contacts an obstacle, t_{obs} , being at the locus $X_{tip,f}(t_{obs})$, which can be calculated from a condition $R_f(t_{obs}) = (1 - \alpha)H$ in Eq. (3.17):

$$t_{obs} = \frac{n}{\Theta U_f} \left\{ \frac{\Theta H}{(\Theta - 1) k_{DL}^{n-1}} \ln \left[\frac{\Theta}{1 + \alpha(\Theta - 1)} \right] \right\}^{1/n}, \quad X_{tip,f}(t_{obs}) = \frac{\Theta(1 - \alpha)H}{1 + \alpha(\Theta - 1)}. \quad (3.19)$$

Similarly, the respective flame tip velocity, $U_{tip,f}(t_{obs})$, can be found from Eq. (3.19). This formulation does not work for $t > t_{obs}$ because the obstacles come to play in this case. Consequently, in order to extend the coalmining fire scenario beyond t_{obs} , the obstacles should be accounted for. Here we recall the Bychkov mechanism of ultrafast flame acceleration in obstructed channels [16]. Adopting a limit of tightly-placed obstacles, $\Delta x \ll \alpha H$, we treat the flow between the obstacles as laminar such that the flame front therein may be taken as locally planar at all times, thus spreading in the y -direction with the laminar flame speed U_f . As the burnt matter expands with a thermal expansion ratio Θ , the flow is pushed out of the pockets. Coming into a central part of the passage, the flow changes its direction and pushes the flame forward in the x -direction towards the exit. This creates a positive feedback between the flame and pockets as the flame is pushed forward, thereby creating new pockets behind it. Considering the flow in the free part of the passage as potential and incompressible, $\partial U/\partial x + \partial V/\partial y = 0$, and a boundary condition $V = -(\Theta - 1)U_f$ at $y = (1 - \alpha)H$, in the burnt gas:

$$(U; V) = \frac{(\Theta - 1)U_f}{(1 - \alpha)H} (x, -y), \quad \frac{dX_{tip,o}}{dt} = \frac{(\Theta - 1)U_f}{(1 - \alpha)H} X_{tip,o} + \Theta U_f. \quad (3.20)$$

Equation (3.20) summarizes the original formulation [16] yielding exponential acceleration, $X_{tip,o} \propto \exp(\sigma t)$, with $\sigma = (\Theta - 1)U_f/(1 - \alpha)H$. It is Re-independent (scale-invariant), with $U_f = \text{const}$. We next revisit it accounting for the DL instability. Namely, we consider $U_{DL}(t)$ obeying Eq. (3.17) until $t = t_{obs}$ such that

$$U_{DL}(t_{obs}) = U_f \left\{ \frac{\Theta H}{(\Theta - 1) k_{DL}} \ln \left[\frac{\Theta}{1 + \alpha(\Theta - 1)} \right] \right\}^{(n-1)/n}. \quad (3.21)$$

Thereafter, we assume U_{DL} remaining at a saturated level of $U_{DL|obs} = U_{DL}(t_{obs})$, Eq. (3.21), because a characteristic flame radius stops growing at this point. Then substituting $U_{DL|obs}$ into Eq. (3.20) yields an evolution equation for a flame tip propagating through an array of obstacles, for $t > t_{obs}$

$$\frac{dX_{tip,o}}{dt} = \frac{(\Theta - 1)U_{DL|obs}}{(1 - \alpha)H} X_{tip,o} + \Theta U_{DL|obs}, \quad t > t_{obs}. \quad (3.22)$$

Integrating Eq. (3.22) with a matching condition $X_{tip,o}|_{t=t_{obs}} = X_{tip,f}(t_{obs})$ yields the solution

$$X_{tip} = \frac{\Theta(1 - \alpha)H}{1 + \alpha(\Theta - 1)} \left\{ 2 \exp \left[\frac{(\Theta - 1)U_{DL}(t_{obs})}{(1 - \alpha)H} (t - t_{obs}) \right] - 1 \right\},$$

$$\frac{dX_{tip}}{dt} = U_{tip} = 2 \frac{\Theta(\Theta - 1)U_{DL}(t_{obs})}{1 + \alpha(\Theta - 1)} \exp \left[\frac{(\Theta - 1)U_{DL}(t_{obs})}{(1 - \alpha)H} (t - t_{obs}) \right]. \quad (3.23)$$

We also determine the flame run-up distance, which is conventionally defined as the distance at which the flame velocity reaches the sound speed of the reactants, c_0 . Namely, Eq. (3.23) gives the run-up time, t_{rud} , as

$$t_{rud} = t_{obs} + \frac{(1 - \alpha)H}{(\Theta - 1)U_{DL}(t_{obs})} \ln \left[\frac{c_0(1 + \alpha(\Theta - 1))}{2\Theta(\Theta - 1)U_{DL}(t_{obs})} \right], \quad (3.24)$$

and substituting t_{rud} , Eq. (3.24) into Eq. (3.23) gives the corresponding flame run-up distance, X_{rud} .

We next extend our analysis to a gaseous-dusty environment by using a modified version of the Seshadri formulation [2] that expresses the laminar flame speed as a function of the local thermal-chemical properties of the gas and dust particles (inert; such as sand, combustible; i.e. coal, and combined) in the form [17]

$$U_{d,f} = U_f \sqrt{\frac{\phi_s}{\phi}} \sqrt{\frac{C_p}{C_T}} \left(\frac{T_f}{T_b} \right)^2 \left(\frac{T_b - T_u}{T_f - T_u} \right) \sqrt{\exp \left(\frac{E(T_f - T_b)}{T_f T_b R_u} \right)}, \quad \phi_s = \frac{\left[\left(\frac{m_{fuel}^m}{M_{CH_4}} \right) / \left(\frac{m_{air}^m}{M_{air}} \right) \right]_{act}}{\left[\left(\frac{m_{CH_4}^m}{M_{CH_4}} \right) / \left(\frac{m_{air}^m}{M_{air}} \right) \right]_{st}}, \quad (3.25)$$

where ϕ_s is the modified equivalence ratio of the dusty-gaseous-air mixture in the presence of particles; M_{CH_4} , M_{air} are the respective molar masses; $m_{CH_4}^m$, m_{air}^m and m_{fuel}^m are the original masses per unit volume for a given equivalence ratio; see also Eqs. (3.7) and (3.8) and the discussion therein.

3.3.2 Effect of gas compressibility. Incompressible formulation above has predicted unlimited flame acceleration, which potentially may promote the flame velocity to near-sonic values, for which the incompressible model is not acceptable. To get rid of such a discrepancy, we next extend the analysis to account for small but finite Mach numbers associated with flame propagation, $Ma(t) = U_{DL}(t)/c_0$. As long as the explosion development process is substantially subsonic, $Ma \ll 1$, the flow in the unburnt gas can be treated as isentropic, with the instantaneous density, pressure and temperature given by

$$\frac{\rho_u(t)}{\rho_0} = \left(1 + \frac{\gamma-1}{2} \frac{u_{z,1}(t)}{c_0} \right)^{2/(\gamma-1)} \approx 1 + Ma(t)(\Theta-1) \left(1 + \frac{Z_{tip}(t)}{h} \right), \quad (3.26)$$

$$\frac{P_u(t)}{P_0} = \left(1 + \frac{\gamma-1}{2} \frac{u_{z,1}(t)}{c_0} \right)^{2\gamma/(\gamma-1)} \approx 1 + \gamma Ma(t)(\Theta-1) \left(1 + \frac{Z_{tip}(t)}{h} \right), \quad (3.27)$$

$$\frac{T_u(t)}{T_0} = \left(1 + \frac{\gamma-1}{2} \frac{u_{z,1}(t)}{c_0} \right)^2 \approx 1 + (\gamma-1) Ma(t)(\Theta-1) \left(1 + \frac{Z_{tip}(t)}{h} \right), \quad (3.28)$$

where $\gamma = c_p/c_v \approx 1.4$ is the adiabatic index and ρ_0, P_0, T_0 are the initial values in the unburnt gas. Instead of the initial thermal expansion ratio $\Theta \equiv \rho_{fuel}/\rho_{burnt}$, here we deal with an instantaneous (reduced) expansion ratio $\vartheta(t) = \Theta - (\gamma-1) Ma(t)(\Theta-1) \{1 + Z_{tip}(t)/h\}$. The continuity equation for small but finite compressibility, $\nabla \mathbf{u} = -(\partial P_u/\partial t)/\gamma P_u$, has the solution in the burnt gas in the form:

$$u_x = -\frac{1}{\gamma P_u} \frac{\partial P_u}{\partial t} \frac{x}{h}, \quad u_z = \left(\frac{1}{\gamma P_u} \frac{\partial P_u}{\partial t} + (\vartheta-1) \frac{U_{DL}(t)}{h} \right) z. \quad (3.29)$$

Substituting Eqs. (3.26)–(3.29) into a modified evolution equation, $Z_{tip} - u_{z,2}(\vartheta(t)) = \vartheta(t) U_{DL}(t)$ [compare with the previous formulation], and further neglecting the 2nd- and higher order terms in Ma , we eventually arrive to the final evolution equation for the flame tip, Z_{tip} , in the form

$$\frac{dZ_{tip}}{dt} = -\chi \frac{\sigma_0^2}{U_{DL}(t)} Z_f^2 + \sigma_1 Z_f + \Theta_1 U_{DL}(t), \quad (3.30)$$

where $\sigma_0(t) = (\Theta-1) U_{DL}(t)/(1-\alpha)H$ is the exponential factor, $\Theta_1 = \Theta - Ma(t)(\gamma-1)(\Theta-1)^2$,

$$\chi = Ma(t) \left[(1-\alpha)^{-1} + \gamma - 1 \right] + \frac{dMa(t)}{dt} \frac{R}{(\Theta-1)U_{DL}(t)}, \quad \sigma_1 = \sigma_0 \left[1 - Ma(t) \left(\frac{\Theta}{(1-\alpha)} + 2(\gamma-1)(\Theta-1) \right) - \frac{dMa(t)}{dt} \frac{R}{U_{DL}(t)} \right].$$

Similar to the incompressible approach, the compressible one, Eq. (3.30), is solved until the instant t_{obs} at which the flame skirt touches an obstacle and after which the Mach number associated with flame propagation, $Ma(t_{obs})$, and the instantaneous global flame velocity, $U_{DL}(t_{obs})$, become constants. With a corresponding flame tip position $Z_{tip,c}(t_{obs})$ for $t > t_{obs}$ Eq. (3.30) is integrated as

$$Z_{tip} = \frac{Z_{tip,2} C_1 \exp[\sigma_2(t - t_{obs})] - Z_{tip,1}}{C_1 \exp[\sigma_2(t - t_{obs})] - 1}, \quad (3.31)$$

where $\sigma_2 = \sqrt{\sigma_1^2 + 4Ma\Theta_1\chi\sigma_0^2}$, $Ma = Ma(t_{obs})$, $C_1 = (Z_{tip,c}(t_{obs}) - Z_{tip,1}) / (Z_{tip,c}(t_{obs}) - Z_{tip,2})$, $Z_{tip,1} = (\sigma_1 - \sigma_2) / (2Ma\chi\sigma_0^2 / U_{DL})$, $Z_{tip,2} = (\sigma_1 + \sigma_2) / (2Ma\chi\sigma_0^2 / U_{DL})$, $U_{DL} = U_{DL}(t_{obs})$.

4.0 RESEARCH FINDINGS AND ACCOMPLISHMENTS

4.1 Experimental Findings

4.1.1 One-compartment setup – Results. The consecutive images in Fig. 7 depict the entire scenario of a venting explosion, both inside and outside the compartment, for the vent area $A_v = 86.6 \text{ cm}^2$.

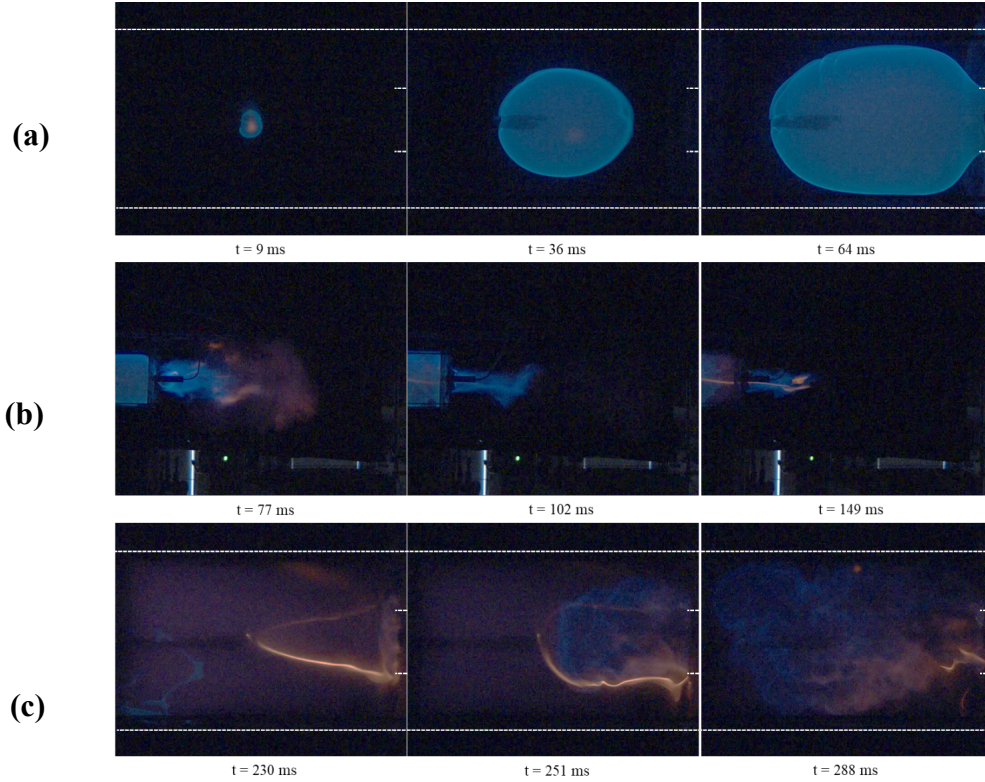


Fig. 7: An overall look of the explosion test from both inside and outside vessel perspectives: (a) Initial flame expansion inside the vessel; (b) the flame overshoot outside the vessel; and (c) flashback inside the vessel.

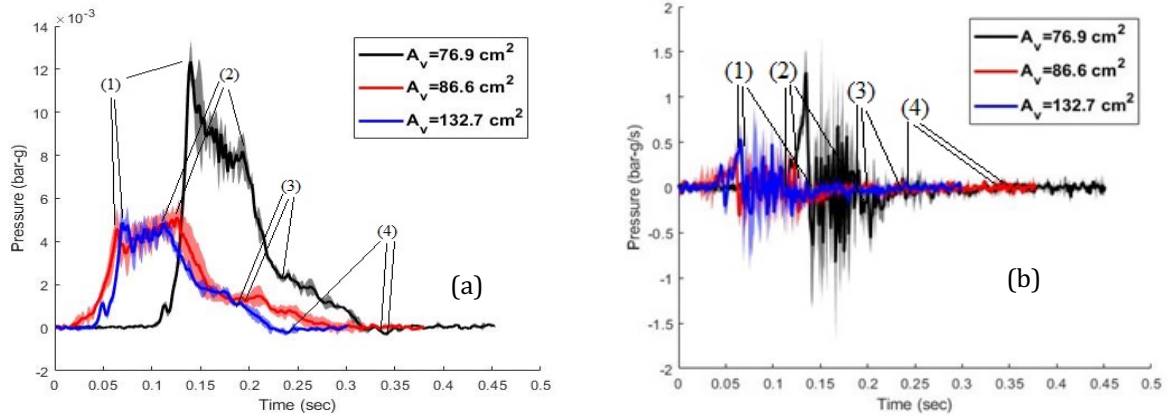


Fig. 8: Evolution of pressure (a) and the rate of pressure (b) for the vented explosion tests of a rich ($\phi = 1.2$) methane-air flame ignited centrally inside a cylinder with the vent areas of $A_v = 67.9, 86.6$ and 132.7 cm^2 .

The white dash lines in Figs. 7a & 7c show the vessel walls (bottom and left) as well as the vent (two shorter lines in the middle). To be more specific, Fig. 7a presents the initial stage of explosion, when a flame spreads inside the vessel. We see here that the embryonic flame initially expands spherically, but subsequently its right side is predominantly drawn towards the vent such that the overall flame front acquires an elongated, ellipsoidal-like shape. The second snapshot in Fig. 7a ($t = 36 \text{ ms}$) corresponds to the first pressure peak, after which the flame oscillations occur as will be seen later, in Fig. 8a. Figure 7b is a sequel of Fig. 7a, showing flame propagation outside the vessel. The first snapshot ($t = 77 \text{ ms}$) corresponds to the second pressure peak. We conclude from the image that the second peak is caused by external explosion, associated with intensive combustion outside the vessel.

Subsequently, amount of remaining fresh gas inside the vessel reduces with the development of the explosion process, so the venting process diminishes thus moderating combustion outside the vessel as seen from the gradual reduction of the external flame length (the maximal external flame length found in this experiment is 54.3 cm). This scenario is reflected in the pressure history as the gradual pressure reduction, see Fig. 8. Further, the external flame comes back into the vessel to continue combustion the fresh mixture, which is still remained inside. Such a flashback process is depicted by the snapshots of Fig. 7c. Most important conclusions can be drawn in terms of peak pressures as external explosion causes the second peak pressure after the start of venting. While Fig. 7 with the discussion above provided a qualitative description of explosion venting, we next quantitatively analyzed this process and its major characteristics. Specifically, Fig. 8 shows the evolutions of the gauge pressure (8a) and its derivative (8b) for rich ($\phi = 1.2$) CH_4 -air combustion inside a cylindrical vessel for various vent areas. The shaded bands attached to the curves depict the deviations obtained within three repetitive experiments. It is seen that maximum pressure and the maximum pressure rise are associated with the smallest vent area, $A_v = 67.9 \text{ cm}^2$. Also, the difference between the cases of $A_v = 86.6 \text{ cm}^2$ and 132.7 cm^2 , is found to be minor, which may mean that the optimal vent area (preventing the further overpressure development) to be around the medium size vent. It is noted that another, smaller pressure peak is observed just before maximum overpressure (the main first peak in the plot). We hypothetically devote this small peak to an onset of diffusional-thermal instability. According to Fig. 8a, the maximum pressure is reached at $\sim 50 \text{ ms}$ after ignition, which is the time when the flame venting has started (see Fig. 7). Therefore, pressure increases from an instant that a flame embryo evolves from the ignition point and the flame surface grows. However, venting prevents further pressure raise. After the first peak, pressure experiences oscillations in all the cases considered. These oscillations correlate with the variations of the flame surface area, which we devote to an interplay between the venting process and formation of a cellular structure of the flame front. Namely, while the cellular formation promotes the total flame velocity and, thereby, pressure

inside the compartment, these effects are diminished by the venting process. It is also seen that the rate of pressure rise towards its maximum exceeds the rate of subsequent pressure drop. This denotes moderation of flame propagation towards the sidewall of the cylinder, due to pull-back of the flame after venting occurs. In Fig. 8b, the maximum rate of pressure increase is seen in the case of $A_v = 67.9 \text{ cm}^2$ and subsequent oscillations of the pressure rate are also seen after venting occurs.

The experimental data for the maximal pressure, P_{max} , and the maximal rate of pressure rise, $(dP/dt)_{max}$, are plotted versus the vent area in Fig. 9. The pressure maxima have been found to be $P_{max} = 12.6, 5.3$ and 5.4 mbar-g for the vent areas $A_v = 67.9, 86.6$ and 132.7 cm^2 , respectively. It is noted that the values of P_{max} for $A_v = 86.6 \text{ cm}^2$ and $A_v = 132.7 \text{ cm}^2$ are very close, however, much smaller than that for $A_v = 69.7 \text{ cm}^2$. This outcome can be devoted to insufficient venting occurring before the flame evolves to a large radius. Similarly, the maximum rate of pressure rise also acquires its largest quantity of $(dP/dt)_{max} = 1.55 \text{ bar-g/s}$ in a compartment with the smallest venting area, $A_v = 67.9 \text{ cm}^2$. The error bars in Fig. 9 show deviations of repeated experiments for each condition. The largest error bar is found in the experiment for $A_v = 132.7 \text{ cm}^2$ that shows less repeatability of such a parameter at large vents, relative to the two smaller vents.

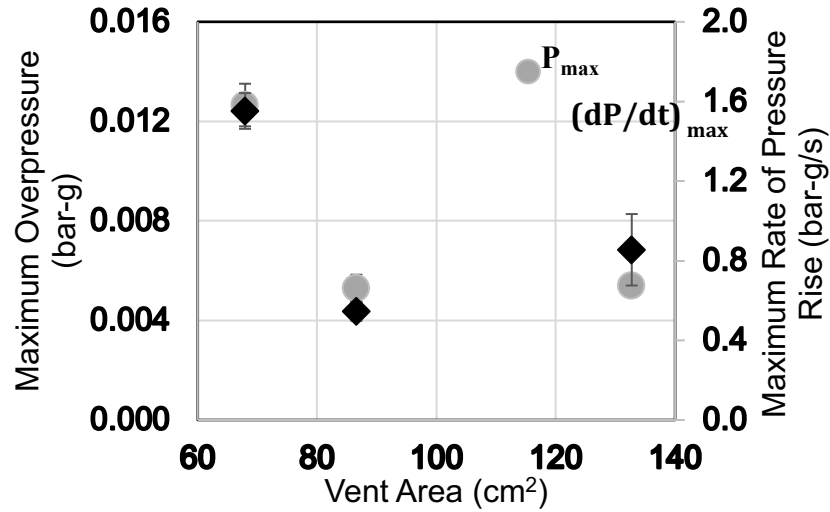


Fig. 9: The maximum overpressures and the rates of pressure rise versus the vent area.



Fig. 10. Images of the flame flashback after combustion is complete inside the vessel for three vent sizes: (a) $A_v = 67.9 \text{ cm}^2$; (b) $A_v = 86.6 \text{ cm}^2$; and (c) $A_v = 132.7 \text{ cm}^2$.

According to recorded flame dynamics videos, one more intriguing feature occurs when the primary combustion process in the vessel is over, namely, the external flame bounces back into the vessel to consume the remaining fuel. This **flashback** is represented in Fig. 10 showing the flame evolution (left to right) after the flame is returned back to the vessel. The flashback incidents in Fig. 10 have been captured after some manipulation of the images to better represent the reaction zones. For the vent areas of $A_v = 86.6$ and 132.7 cm^2 , the flashback occurs in the time intervals between 150 and 180 ms after ignition, while for the smallest vent area, $A_v = 67.9 \text{ cm}^2$, it occurs at circa 240 ms.

The color snapshots of Fig. 11 show the evolution of a centrally-ignited, CH_4 -air rich-premixed ($\phi = 1.2$) flame for three various vent sizes under consideration. The white dashed lines at the bottom and top denote the walls of the vessel, while the other two dashed lines in the middle show the location of the vent. It is seen that a flame embryo expands spherically for a short time after ignition until venting comes into play and sweeps the flame to the vent panel section such that the flame front evolves to acquire an ellipsoidal-like shape. During such a spherical-to-ellipsoidal transition, small bump(s) is/are formed on the flame front. We devote this bump formation to the non-unity Lewis number effects, because such rich CH_4 -air combustion is intrinsically non-equidiffusive. Deviation from an ideally-spherical shape of the flame front increases with flame propagation. After the flame tip on the right reaches the vent, and venting of the burned gas starts, the flame tip on the left is drawn to the exit, thereby moderating flame spreading towards the blocked end of the cylinder. As a result, the venting flow dynamics is coupled to the previously-formed bumps on the flame front as well as flame propagation towards the blocked end of the cylinder, thereby yielding complicated flame-flow interaction. During this process, the flame surface is noticeably distorted, with more cells formed at the left segment of the flame. Another interesting observation, Fig. 8b, is that for a vent of area 86.6 cm^2 , the flame started to evolve extremely belatedly as compared to the other two vent conditions. In the present work, the flame dynamics is quantified by means of the evolutions of the flame tip position and velocity, and the acceleration rate (if any). Due to central ignition (CI), the flames in the compartment propagate into two opposite directions: (i) towards the vent (right on the images) and (ii) in the opposite direction, towards the wall (left on the images).

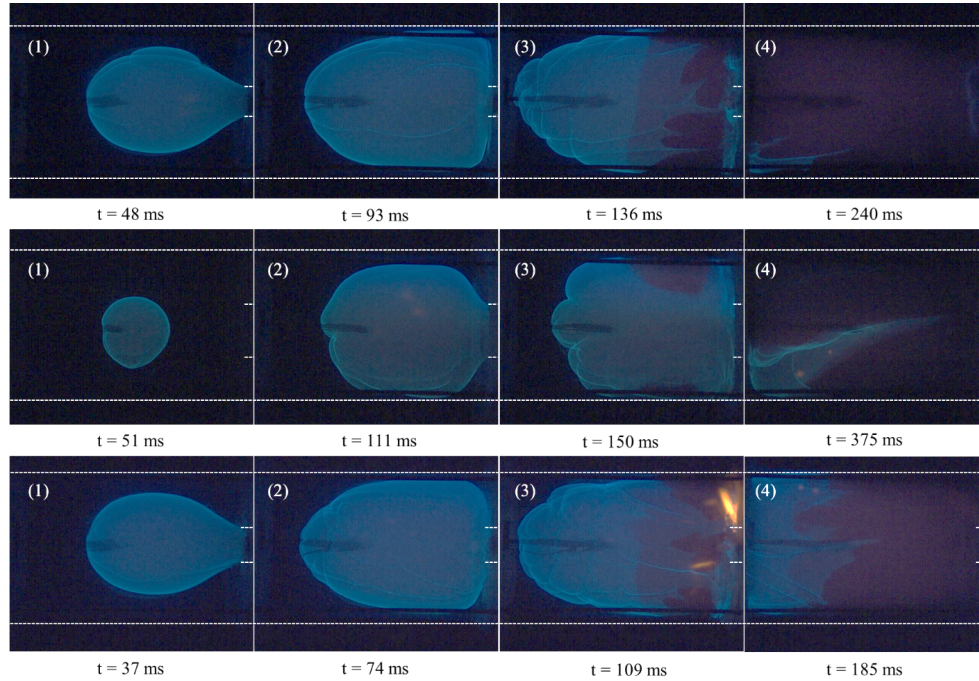


Fig. 11: Evolution of a rich ($\phi = 1.2$) CH_4 -air premixed flame inside the cylinder with three different vent areas: (a) $A_v = 67.9 \text{ cm}^2$; (b) $A_v = 86.6 \text{ cm}^2$ and (c) $A_v = 132.7 \text{ cm}^2$.

Figure 12 presents the flame location and velocity vs time for the flame evolutions in both directions. It is clearly seen that flames move faster towards the vent than to the wall because of the pressure release created by venting. In addition, the reduction of the flame surface area results in a nozzle flow effect thus creating fast flame spreading towards the vent. On the other hand, as the flame front expanded gradually, a back flow from the vent pulled the flame back. We have found that the tip of the flame segment on the left moved with an almost constant velocity towards the sidewall, as followed from a linear fit of the flame position. On the other side, the flame segment propagating toward the vent experiences exponential acceleration. As a result, the highest maximum pressure is observed in the case of the smallest vent area. For all three cases, pressure evolutions experience two major peaks, associated with the instants (i) when the maximum surface area of the flame front in the chamber is reached and (ii) when an external explosion occurs due to the venting of unburned gasses, respectively. Subsequently, a flashback is observed after the external explosion, constituting the key outcome of the present work. The flame tip velocities show two general trends, namely, the flames spread almost steadily towards a blocked side of a compartment, but accelerate exponentially when propagating towards a vent, which sheds the light on the fire/explosion safety applications.

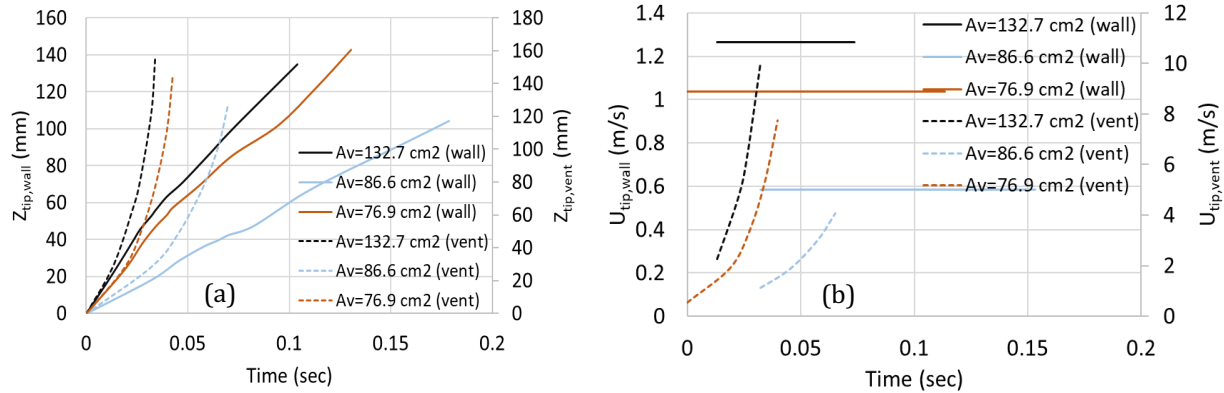


Fig. 12: The position (a) and velocity (b) of a flame tip propagating towards the blocked end as well as the vent directions for three vent sizes: $A_v = 67.9, 86.6$ and 132.7 cm².

These findings have been published in Journal of Loss Prevention in the Process Industries [21].

4.1.2 Two-compartment setup – Results. We next performed a similar experimental investigation in a two-compartment setup of Fig. 3. In particular, Fig. 13 shows a typical flame evolution in the second compartment, occurring when the fuel-air mixture in the first compartment is partially consumed.

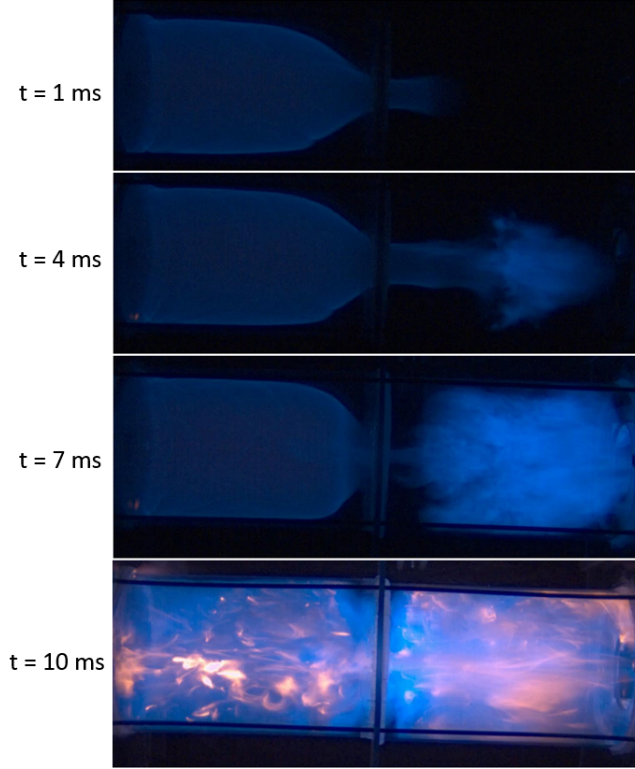


Fig. 13: Stages of stoichiometric CH₄-air combustion in the second compartment of a two-compartment vessel with a vent area of $A_v = 86.6 \text{ cm}^2$.

Upon entering the second compartment, the first vent acted like a nozzle, contracting the flame and pushing the flame to the second compartment, with a high velocity. When the pushed flame reached the second vent, it expanded in the radial direction rather than continuing to discharge out of the vessel. This is because there is still a big portion of the unburned mixture in the second compartment. A flame with such a velocity consumes the fresh fuel mixture in the second compartment and, at the same time, jumps back to the remaining fresh fuel in the first cylinder. Such a jet-flame ignition (depicted in the $t = 10 \text{ ms}$ snapshot of Fig. 13 and resulted in rapid combustion in two compartments simultaneously) creates a very high pressure raise. It is noted that the scenario depicted in Fig. 13 is qualitatively similar for each equivalence ratio; though the quantitative parameters obviously differ.

4.2 Computations vs Experiments – Validation of the Explosion Models.

In the past, the team of *Dong* reported a combined experimental and computational investigation of vented explosions of a hydrogen-air mixture in a cylinder of length 100 cm and diameter 18 cm [22]. Consequently, we started with employing the EVA to predict the pressure of hydrogen-air explosions in such a cylindrical enclosure. The initial conditions were taken as $P_{u,0} = 1 \text{ atm}$ and $T_{u,0} = 25^\circ\text{C}$. Figure 14a compares the EVA results with the experimental data and the CFD modelling of [22].

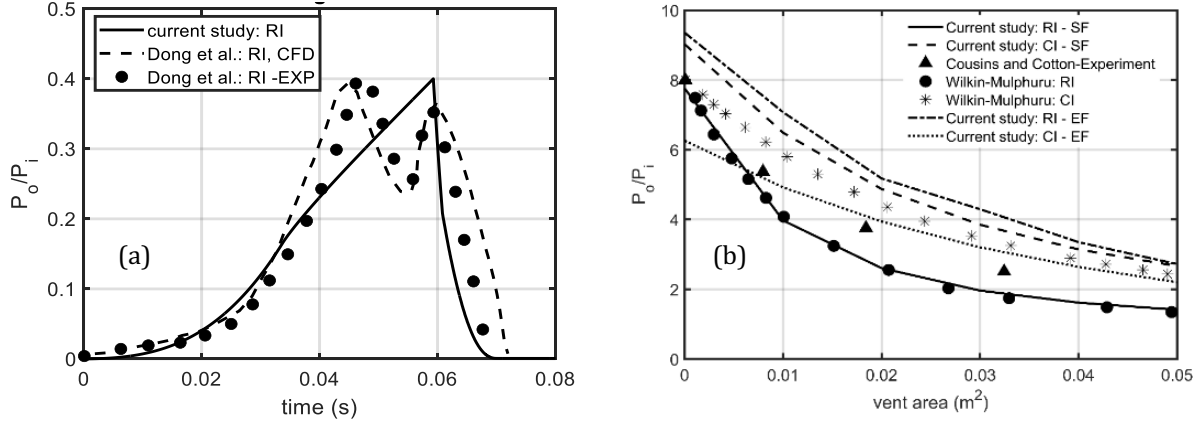
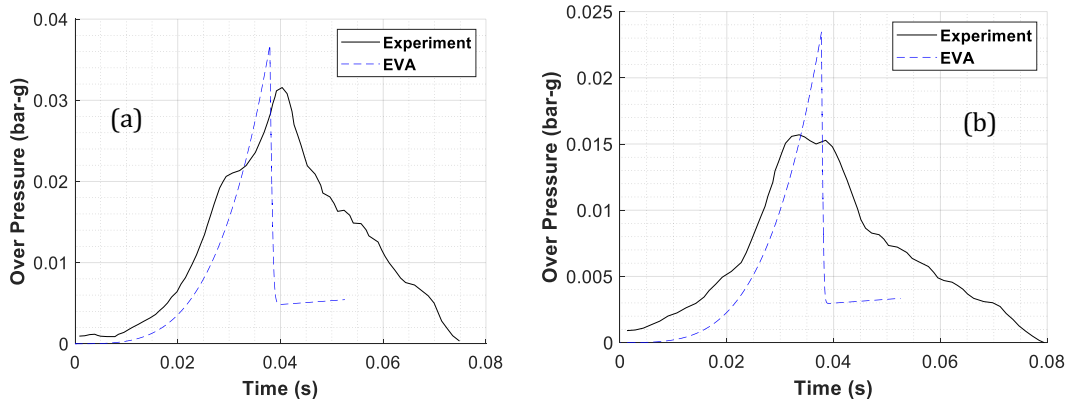


Fig. 14: Validation of the EVA for H_2 -air explosions in vented cylindrical enclosures. (a) Comparison with Ref. [22]: the scaled pressure P_0/P_i vs time in a cylinder of length 100 cm and diameter 18 cm. (b) The maximum scaled peak pressure vs the vent area in a of length 77.5 cm and diameter 59.4 cm.

Specifically, time evolution of the scaled pressure, P_0/P_i , in the case of rear ignition (RI) is depicted in Fig. 14a with good agreement between the EVA and Ref. [22] seen. In addition, we have tested how the flame shape and the ignition location influence the accuracy of the EVA predictions. This is shown in Fig. 14b, where the maximum peak pressures are presented versus the vent area, with two options for the flame morphology: the spherical and the ellipsoidal flame shapes for both central ignition (CI) and rear ignition (RI). Here, the EVA results are compared with the experimental data, shown by the markers. Again, we see good agreement between the EVA and the experiments in Fig. 14b.

However, unlike Fig. 14 devoted to H_2 -air explosions, in this project we mainly focus, computationally and experimentally, on vented explosions of (stoichiometric) CH_4 -air mixtures, with various vent areas considered. Obviously, the model geometry imitates that of our experiments (see also Ref. [21]) with RI employed as the location of ignition. Below, the corresponding pressure evolutions will be shown and validated by the experiments [21].

4.2.1 Pressure Evolution. Figure 15 shows overpressure vs time for various vent areas, namely, $A_v = 67.9 \text{ cm}^2$, 86.6 cm^2 , and 132.7 cm^2 in Fig. 15 (a–c, respectively). In all three cases, the EVA predictions are validated by the experiments [21]. Specifically, in Fig. 15a, transient pressure, recorded from the experiment, and the EVA simulation results matched initially at the onset. Quantitatively, the peak pressures were 0.036 bar-g and 0.031 bar-g for the EVA and the experiments, respectively. While the maximum overpressure from the EVA appeared 14% higher than that reported in the experiments; in fact, such an over-prediction is good for safety purposes (the key point of the EVA is to predict the worst scenario without underestimating the risks). The EVA simulations attained the maximum overpressure quicker as compared to the experiments, which shows some timing discrepancy.



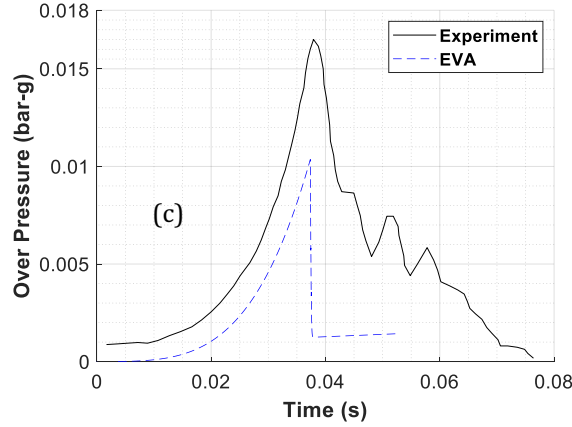


Fig. 15: Time evolution of overpressure for stoichiometric CH₄-air explosions in a cylindrical enclosure with the vent areas 67.9 cm² (a), 86.6 cm² (b), and 132.7 cm² (c).

It is also noted that after attaining the maximum overpressure, the pressure history results from the EVA stopped matching the experimental results; such a deviation can be due to combustion instabilities or other factors from the experiments not accounted in the EVA. Figure 15b is a counterpart of Fig. 15a for the medium vent area, $A_v = 86.6$ cm². Both these figures show qualitatively similar trends. The maximum overpressures for the middle vent case, Fig. 14b, are 0.023 and 0.015 bar-g from the EVA and the experiments, respectively. Here, the EVA over-predicted the experimental values peak pressure by 53%—much stronger as compared to the 14% in the small vent case, Fig. 15a. Regarding Fig. 14b, it is also noted that the time when the EVA attained the peak pressure fits the experiment peak pressure time well. It is also seen that the EVA transient pressure results of Fig. 15b match the experimental values until the peak pressure is attained; thereafter, the EVA pressure dropped and transitioned to an almost constant value. Finally, when the vent area has been further increased, to $A_v = 132.7$ cm² (the large vent case, Fig. 15c), the EVA pressure history and timing generally match experimental results before attaining the peak pressure. Quantitatively, the EVA predicted the overpressure of 0.01 bar-g in this case, while the experimental value was 0.016 bar-g.

4.2.2 Maximum overpressure. It is recalled that the EVA uses the laminar flame velocity as an input parameter. While previously we employed this value as that tabulated from the literature, hereafter we call a commercial one-dimensional (1D) package Cantera as a subroutine of the EVA to calculate the laminar flame velocity by solving a 1D eigenvalue problem. As a result, the Cantera software has been integrated with the EVA—in order to be able to compute the laminar flame speeds by means of Cantera and, thereby, provide an alternative to the laminar flame velocity correlations originally used in the EVA. This integration was implemented at the very beginning of the present study in order to enhance the versatility of the EVA code, making it able to be used for a wider range of fuels.

Figure 16 compares the peak pressures obtained from the original EVA (blue) as well as from the EVA with Cantera (black) with those from our experiments [21] (red) for various vent areas. The results calculated by means of the NFPA 68 standards [23] are shown by the green circles. The results are presented in both the normal, Fig. 16a, and the semi-logarithmic, Fig. 16b, scales. It is visually seen from Fig. 16 that the EVA predictions generally agree with the experiments [21]. Moreover, it is clearly seen that both EVA cases (with and without Cantera) show much better agreement with the experiments [21] than the NFPA 68 standards [23]. The corresponding peak pressure values as well as the errors of the approaches are tabulated in Table 1. It is seen that the EVA-Cantera model yields higher overpressures than the original EVA. Obviously, this is because Cantera provided the higher laminar flame velocity value as compared to the original EVA correlations. It is seen that it was particularly beneficial to use the integrated EVA-Cantera model for the large vent area case, $A_v = 132.7$ cm²: it predicted the experimental peak pressure better than the original EVA model in this

case. In contrast, for other two cases of the medium and small vent areas, 86.6 cm² and 67.9 cm², the original EVA model predicted the experiments [21] better than the integrated EVA-Cantera.

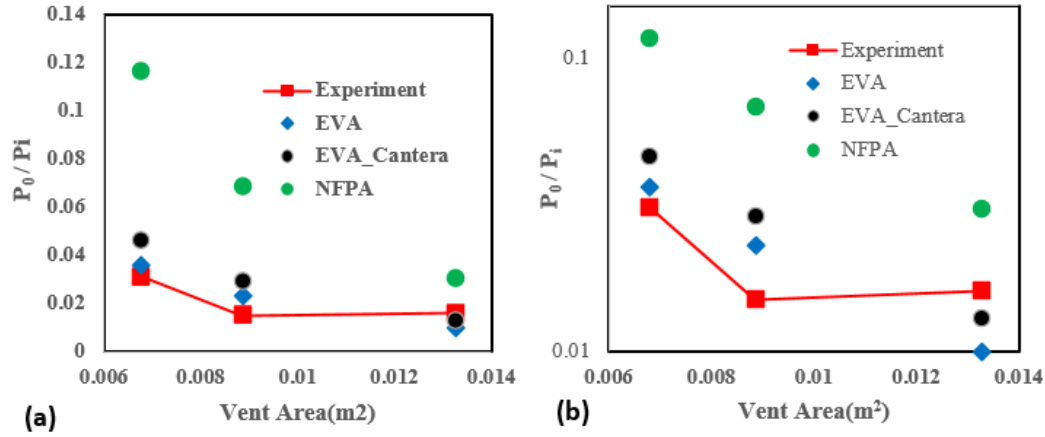


Fig. 16: The peak pressures vs the vent area in the normal (a) and semi-logarithmic (b) scales: Validation of the EVA without (blue diamonds) & with (black circles) Cantera by the experiments [1] (red squares). The green squares show the results calculated from the NFPA 68 standards [23].

Table 1. The peak pressures as well as the errors of the approaches for the rear-ignited (RI) stoichiometric CH₄-air explosions in the cylindrical enclosures.

Vent Area (cm ²)	Peak Pressure (bar-g)			Error (%)	
	Experiment	EVA	EVA + Cantera	EVA	EVA + Cantera
$A_v = 67.9$ —the small vent (SV)	0.031	0.036	0.046	16.12	48.39
$A_v = 88.6$ —the medium vent (MV)	0.015	0.023	0.029	53.33	93.33
$A_v = 132.7$ —the large vent (LV)	0.016	0.010	0.013	37.5	18.75

It is recognized that a reader may treat the percentage errors in Table 1 as discouragingly large. It is noted, in this respect, that the NFPA 68 Standards [23] (which are accepted in the literature and fire safety community) provide even worse agreement and larger errors than the EVA, see Fig. 16. Supposedly, this is because quantitative fire safety science yet shows lack of accuracy, being qualitative rather than quantitative. In fact, when predicting, here we consider a "worst case" scenario (to be on a safe side) rather than the practical reality. Regarding Fig. 16, it is also pointed out that the normalized pressures (scaled by the initial pressure) are presented, while a more accurate quantitative analysis would need to deal with the dimensional values, thereby having the initial pressure as one more parameter of the problem. It is nevertheless noted that the computational and experimental pressure results in Fig. 16 (except for the NFPA ones) do not exceed the maximum explosion pressures of Fig. 15.

These findings have been published in FIRE [24] and disseminated at 37th Int. Pittsburgh Coal Conference [25], 12th National Combustion Meeting [26] and 42nd Combustion Institute's Eastern States Section's Technical Meeting [27].

4.2.3 Validation of the EVA by the two-compartment experiments. Eventually, we extended the EVA platform to model a two-compartment configuration of Fig. 3. In this respect, Fig. 17 presents the pressure evolutions in the two-compartment experiments for the lean ($\phi = 0.8$), stoichiometric ($\phi = 1$) and rich ($\phi = 1.2$) CH₄-air explosions as well as the respective EVA predictions. As compared to the single-cylinder case, the pressure results are an order of magnitude higher in the two-

compartment vessel. In each scenario, the EVA predicted the explosion scenario along with the peak pressures very well, provided that a suitable turbulence factor is chosen.

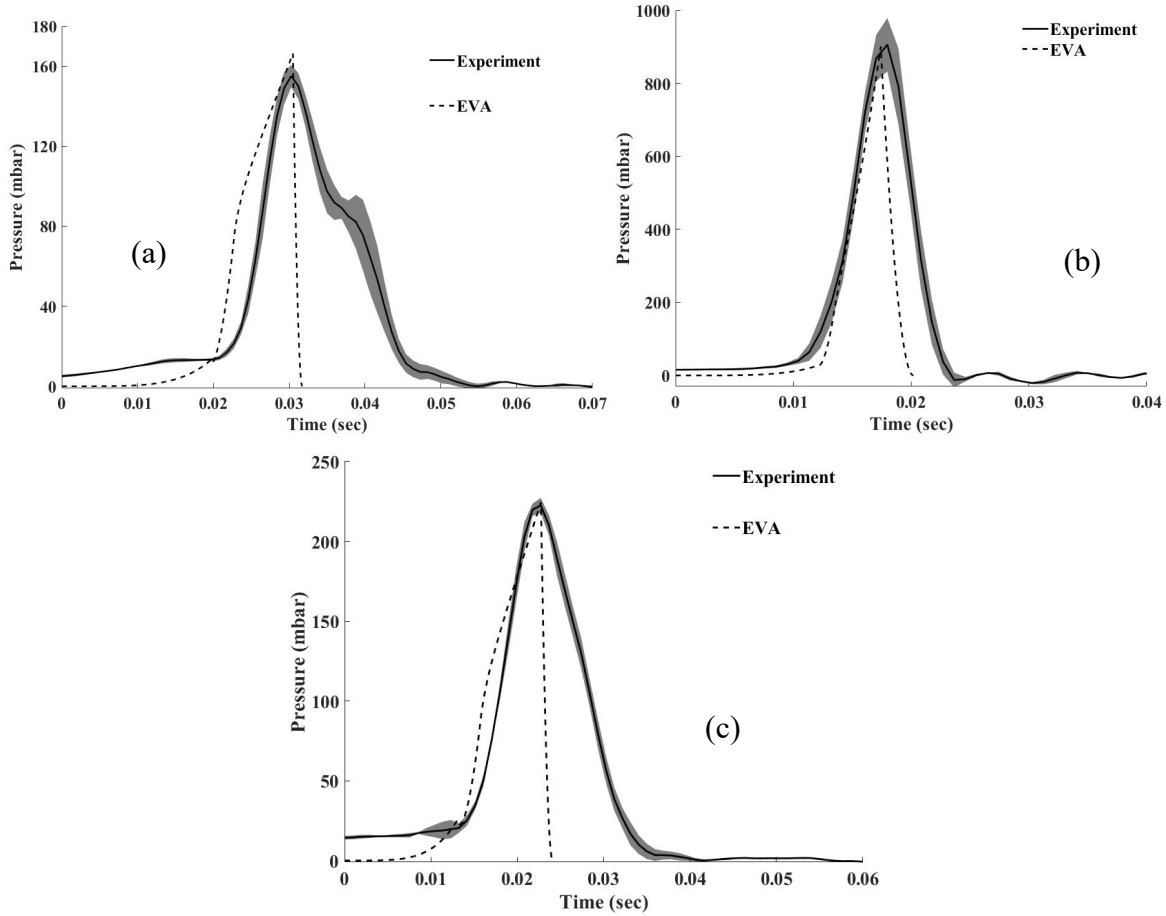


Fig. 17: Pressure evolution of the (a) lean ($\phi = 0.8$), (b) stoichiometric ($\phi = 1$) and (c) rich ($\phi = 1.2$) methane-air explosions in two compartment vessel with a medium vent ($A_v = 86.6 \text{ cm}^2$).

The turbulence factor values chosen for the two-compartment experiments are 2.1, 4 and 1.5 for the $\phi = 0.8$, 1 and 1.2 CH_4 -air simulations, respectively. The reason the turbulence factor for a rich mixture is lower than that for a lean mixture is because the rich mixture has higher thermal-chemical property values which leads, intrinsically, to higher flame speeds for rich as compared to the lean. The reason that stoichiometric mixture has the highest turbulence factor is a stronger explosion originated in the second compartment. For the lean/rich mixtures, sudden explosions were weak.

As a result, we have showcased the capability of using the EVA model [3,4] to predict the pressure evolution in the process of CH_4 -air explosions in vented cylindrical vessels. The EVA was validated by the experimental measurements [21,22]. The EVA over-predicts the peak pressure for small and medium vent area of 67.9 cm^2 and 86.6 cm^2 but under-predicts it when the vent area is as large as 132.7 cm^2 . This might have resulted from the combustion instabilities or other factors not accounted by the EVA. Regarding the pressure evolution with time, for a small vent, 67.9 cm^2 , the EVA predicted faster pressure raise than that in the experiments [21], while for the 86.6 cm^2 and 132.7 cm^2 vent areas, the EVA results generally agree with the experimental data. Also, Cantera was integrated with the EVA to compute the laminar flame velocity. Overall, the EVA is proven to be an acceptable model as its results have good match with the experimental values. This therefore demonstrate the usability of the EVA in determining the peak pressures of gas explosions in cylindrical enclosure.

4.3 Analytical Findings

4.3.1 Analytical results – Gaseous environment. Figure 18 presents evolutions of the flame tip position (18a) and its velocity (18b) for stoichiometric CH₄-air combustion in a passage of half-width $H = 1.05$ m. It is seen that while the compressible theory agrees very well with the incompressible one at an early stage of combustion, the effect of compression comes to play later on, mitigating the flame propagation velocity as compared to the incompressible approach. Specifically, the first nonlinear term in Eq. (3.30) becomes important soon and moderates the flame acceleration trend, from the exponential one, according to the incompressible theory, to slower linear acceleration. Moreover, this nonlinear term breaks the compressible formulation for all blockage ratios such that flame evolution eventually deviates from the incompressible prediction quite soon, so flame acceleration starts to slowdown. For this reason, for the rest of this study we selected a better validity range of both the case of $\alpha = 0$, i.e. the channel is unobstructed, or the event of $\alpha = 1/3$. From a practical viewpoint, the blockage ratios of $\alpha = 1/2$ and $2/3$ are unlikely, however, we also consider them here keeping in mind the worst-case safety scenario.

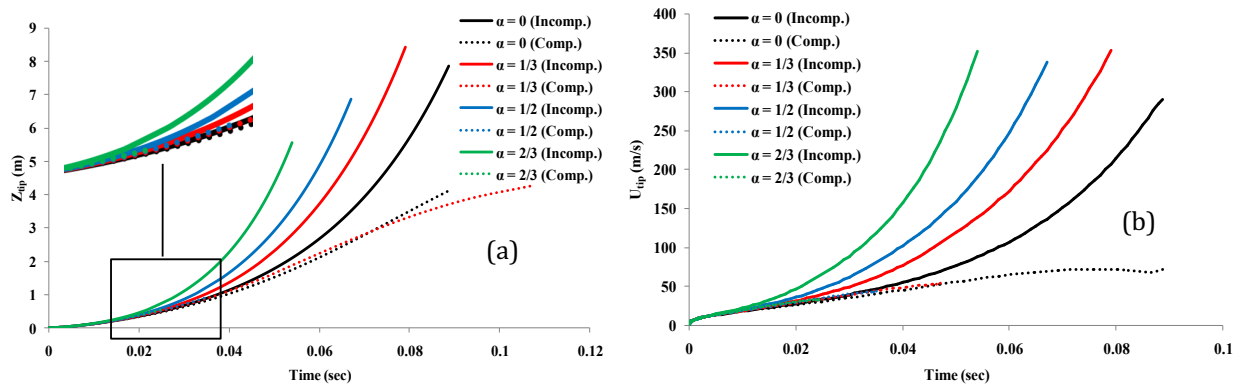


Fig. 18: Evolution of the flame tip for stoichiometric CH₄-air combustion with various mining blockage ratios: $\alpha = 0, 1/3, 1/2, 2/3$. (a) position, Z_{tip} , and (b) velocity, U_{tip} .

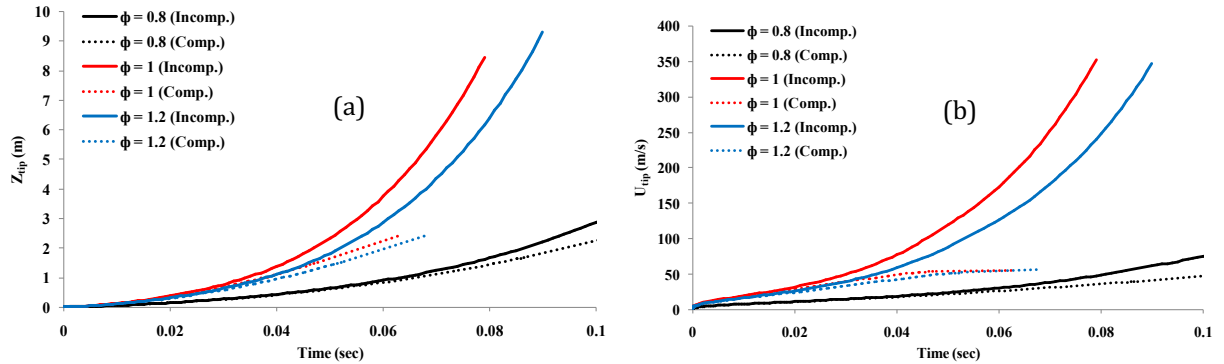


Fig. 19: Evolution of the flame tip for CH₄-air combustion at various equivalence ratios: $\phi = 0.8; 1; 1.2$, with a fixed blockage ratio of $\alpha = 1/3$. (a) position, Z_{tip} , and (b) velocity, U_{tip} .

Figure 19 is a counterpart of Fig. 18 but with a fixed blockage ratio of $\alpha = 1/3$ and various equivalence ratios, $\phi = 0.8, 1, 1.2$. It is seen that gas compression moderates flame acceleration, and this effect is stronger for the rich or stoichiometric conditions. For a lean mixture, the compressible and incompressible theories agree well at the initial stage of a combustion process, however, both trends deviate noticeably at a later stage of the process. Indeed, here the effect of gas compression dominates over that of flame acceleration and reduces the flame velocity, moving us to a conclusion

that Eq. (3.31) might over-predict the impact of gas compression. We next scrutinize the impact of the blockage ratio α . Namely, Fig. 20 compares the $\alpha = 1/3$ case to the unobstructed conduit case ($\alpha = 0$) for $\phi = 0.8, 1, 1.2$. Unlike the incompressible theory, the effect of α appears minor within the frame of the present compressible theory. This is seen when comparing the incompressible results of Fig. 20 to the stoichiometric flames of Fig. 18a with $\alpha = 0$ and $1/3$. Moreover, Fig. 20 also shows that as the premixture conditions get closer to stoichiometry, the blockage ratio effect is diminished slightly compared with the lean mixture. This is due to the fact that the nonlinear term in Eq. (3.30) and the second term become dominant faster, strengthened by Θ and the instantaneous global flame speed U_{DL} at the conditions closer to stoichiometry. Such a correlation diminishes the role of the blockage ratio for “compressible” flame propagation.

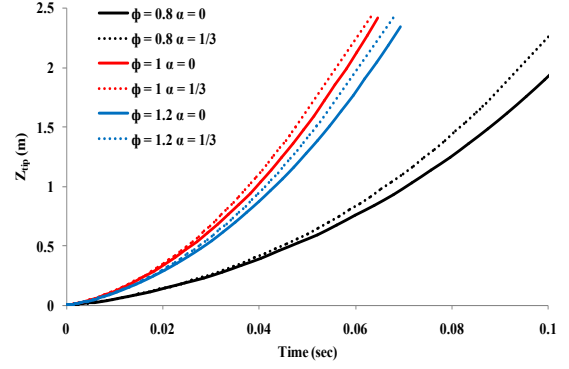


Fig. 20: Evolution of the flame tip position, Z_{tip} , in the passages of blockage ratios $\alpha = 0$ & $1/3$ for CH_4 -air burning with $\phi = 0.8; 1; 1.2$.

4.3.2 Analytical results – Dusty-gaseous environment. Similar what we previously did with the incompressible analysis, we followed the same manner here. Namely, starting with the homogeneous gaseous combustion, we next extend the analysis to account for the presence of dust particles in a coalmining environment by means of the Seshadri formulation [2]; see Eqs. (3.7), (3.8), (3.9) and the discussion therein. Specifically, we considered combustible and inert dust particles as well as their combinations to consider slightly-lean ($\phi = 0.7$), CH_4 -air flames. On the one hand, combustible particles (such as coal dust) release heat into a gaseous environment during their volatilization process, thereby facilitating the combustion process. On the other hand, the presence of inert dust particles (such as sand) or the heat gained by combustible particles may moderate flame propagation.

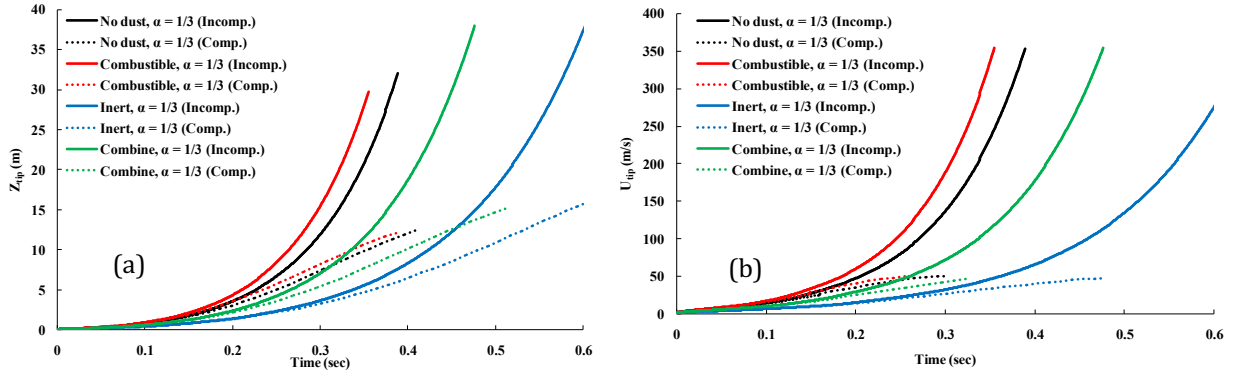


Fig. 21: Evolution of flame tip for lean ($\phi = 0.7$) CH_4 -air combustion, with and without dust particles (inert, combustible, and combined) of radius $r_s = 75 \mu\text{m}$ and concentration $c_d = 120 \text{ g/m}^3$ in a passage with a blockage ratio of $\alpha = 1/3$. (a) position, Z_{tip} , and (b) velocity, U_{tip} .

Figure 21 employs the dust particles of radius $r_s = 75 \mu\text{m}$ and concentration $c_d = 120 \text{ g/m}^3$, as well as the case of no particles. Here, the blockage ratio is $\alpha = 1/3$. Again, it is seen that gas compression moderates flame acceleration in all the cases considered. Presence of dust impacts flame acceleration, specifically, while combustible dusts facilitate the combustion process, addition of inert or combined dust reduces the flame velocity. However, the deviations from the case of no particles are reduced when the account of gas compression is incorporated in the analysis. Figure 21 employs the dust particles of radius $r_s = 75 \mu\text{m}$ and concentration $c_d = 120 \text{ g/m}^3$, as well as the case of no particles. Here, the blockage ratio is $\alpha = 1/3$. Again, gas compression moderates flame acceleration in all cases.

Presence of dust impacts flame acceleration, specifically, while combustible dusts facilitate the combustion process, addition of inert or combined dust reduces the total flame velocity. However, the deviations from the case of no particles are reduced when the account of gas compression is incorporated in the analysis. Finally, the size of the particles has been reduced, from $r_s = 75 \mu\text{m}$ to $r_s = 10 \mu\text{m}$, with the results presented in Fig. 22. All other parameters such as the dust concentration as well as the blockage and equivalence ratios, α and ϕ , are kept the same in Fig. 22 as in Fig. 21. It is seen that similar to the case of $r_s = 75 \mu\text{m}$, the influence of gas compression is also significant here. However, the plots in Fig. 22 deviate from each other more noticeable. While combustible particles facilitate flame propagation and the inert particles moderate this process, it is interesting that the combined dust, in contrast to the case of $r_s = 75 \mu\text{m}$, promotes flame acceleration according to the compressible formulation. This certifies agreement between the two theories, even though not quantitatively but qualitatively. This finding shows that the particle size impacts the fire scenario and smaller particles may facilitate flame acceleration as compared to the case of larger particles. The maximal flame tip velocities in Fig. 22, in the cases of no dust and of combined dust, are almost the same but flame acceleration is slower without dust.

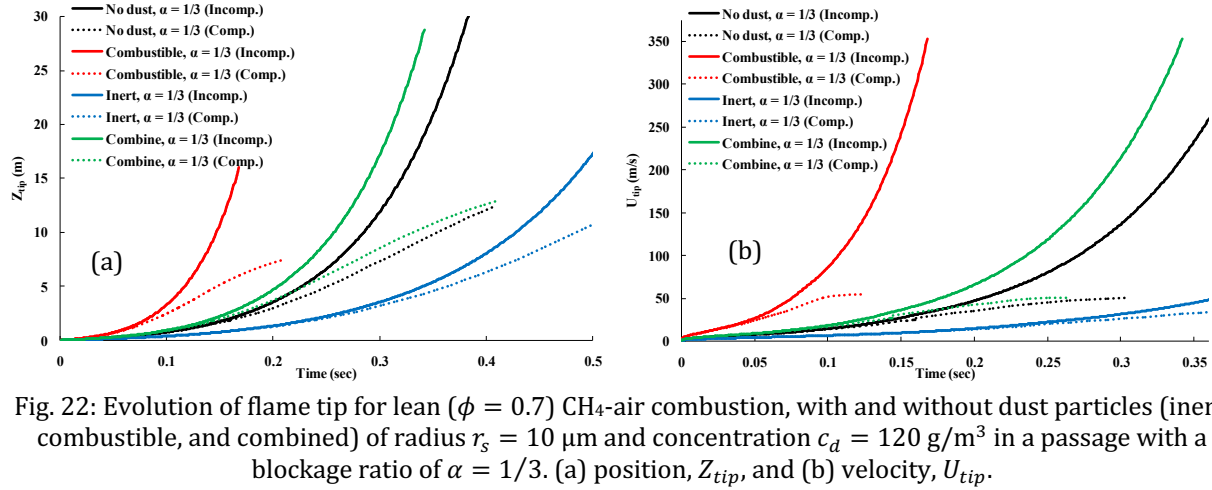


Fig. 22: Evolution of flame tip for lean ($\phi = 0.7$) CH_4 -air combustion, with and without dust particles (inert, combustible, and combined) of radius $r_s = 10 \mu\text{m}$ and concentration $c_d = 120 \text{ g/m}^3$ in a passage with a blockage ratio of $\alpha = 1/3$. (a) position, Z_{tip} , and (b) velocity, U_{tip} .

In summary, our analysis demonstrated that gas compression moderates flame acceleration notably as compared to the incompressible formulation. The impact of the blockage ratio also weakens in with gas compression. As expected, the combustible dust is shown to promote flame acceleration, while the inert particles diminish it. The role of the particle size appears important, and the smaller the dust the stronger the effect is.

Finally, it is recalled that among four distinguished components of the project, the analytical part is a major stand-alone solution element, but to make an overall approach integrative, we have performed multiple validations, by comparing (when applicable) the theory, modelling and experiments to each other as well as to the modelling and experiments available in the literature, as summarized below.

These findings have been published in Fluids [28] and disseminated at 27th Int. Colloquium on the Dynamics of Explosions and Reactive Systems [29], 11th National Combustion Meeting [30], 44th AIAA Dayton-Cincinnati Aerospace Sciences Symposium [31] and 94th Annual Meeting of the West Virginia Academy of Science [32].

4.4 Theory vs Experiments and Modelling – Validation of the Explosion Models.

As was originally planned, whenever it was possible, we have eventually compared our analytical predictions with the experimental component of this project, see also Ref. [21], as well as with the data available in the literature such as the experiments [33] and the numerical simulations (FAST &

ALLA) from the recent Alpha Foundation project [34]. Specifically, the comparison with the literature results are shown in Figs. 23 & 24 below, where the flame tip velocity is shown versus the flame tip position, for various blockage ratios, such that the linear trend represents exponential acceleration.

4.4.1 – Comparison with the literature results. The simulation results [34] are shown by circles while the square markers present the experimental data [33]. The solid/dashed lines are devoted to the theoretical predictions. We have been pleased to observe reasonably good quantitative agreement between the 2D theory and the literature data. As for the cylindrical theory, our qualitative linear theoretical trend fits that of the markers very well.

The majority of these findings have been published in *Physics of Fluids* [35] and disseminated at 37th Int. Pittsburgh Coal Conference [36] and 42nd Combustion Institute's Eastern States Section's Technical Meeting [37].

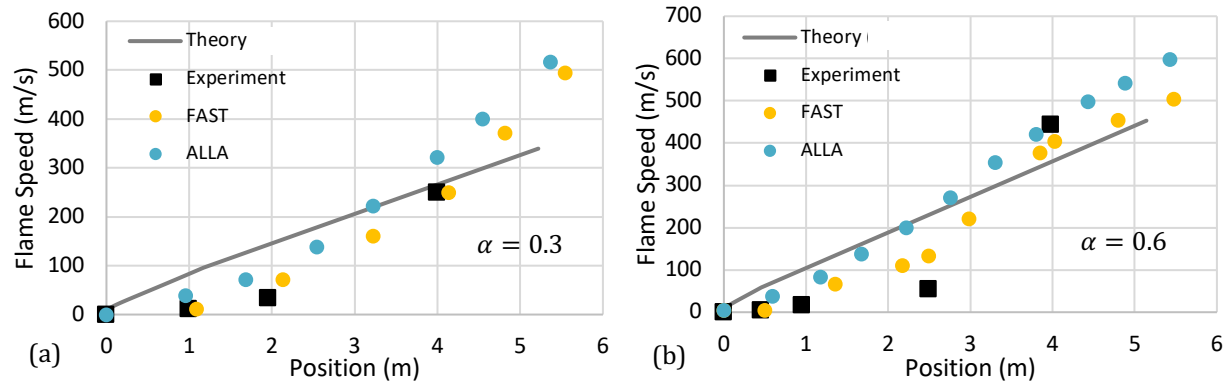


Fig. 23: Comparison of our theoretical formulation with experiments [33] and computational simulations [34] (FAST, yellow, & ALLA, blue): the flame tip velocity vs its position for the blockage ratios $\alpha = 0.3$ (a) & 0.6 (b).

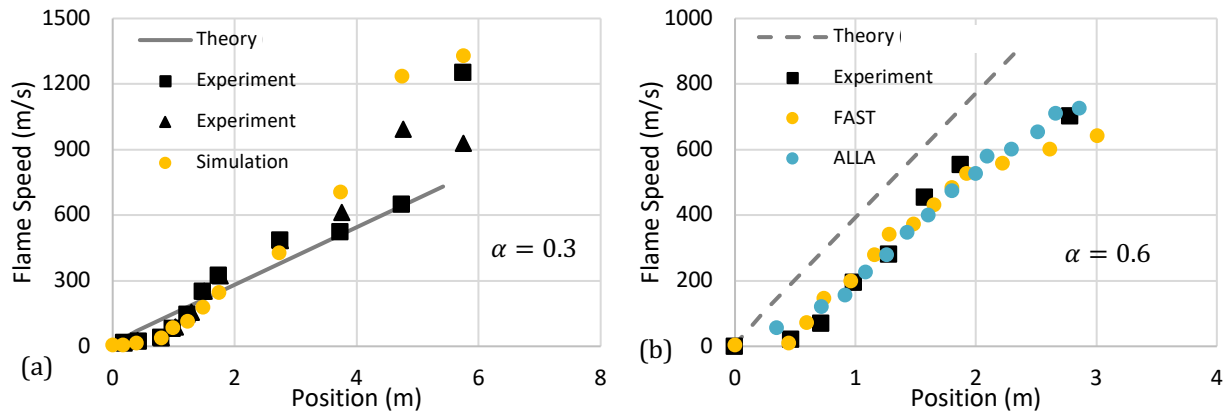


Fig. 24: Comparison of our theoretical formulation with experiments [33] & computational simulations [34]: the flame tip velocity vs its position for the blockage ratios $\alpha = 0.3$ (a) & 0.6 (b).

4.4.2 – Comparison to our experiments. In fact, in all fire scenarios considered here, the so-called finger flame acceleration (FFA) mechanism is dealt with. First, in all conditions of the vented gas explosion experiments, the flame propagated accordingly to this acceleration mechanism. For this reason, the effect of boundary conditions that were assumed in FFA was investigated. Finally, obstacles were added into geometry where its effect on FFA was scrutinized. The flame accelerated in an exponential manner and, as it was also highlighted by Bychkov *et al.* [16,18], this acceleration is scale invariant. Therefore, acceleration rates will be a reasonable approach to compare the theoretical formulation with experiments and simulations conducted in the present project. As soon as the flame tip follows the trend $A \exp(\sigma t)$, where A is constant and t is time, σ gives the exponential acceleration factor (in

s^{-1}). These values were extracted from the experiments and also from the simulations. Specifically, Fig. 25a compares the acceleration rates of rear-ignited methane explosions in extended cylinder (60 cm in length) to that predicted by the theory. Qualitatively, the theoretical and experimental results are in good agreement. Indeed, both theory and the experiments show that the highest acceleration rate occurs when the mixture is stoichiometric and this is followed by the rich mixture. Quantitatively, the acceleration rate factors obtained from theory are higher than those obtained from the experiments in the cases of stoichiometric and rich explosions. Presumably, the theory overpredicts the DL instability in these conditions. For lean mixtures, both acceleration rate coefficients are in a reasonably good agreement with relative difference in the range of 9.7~24.6% for all vent areas. Finally, the theory was compared to the simulations. Specifically, the acceleration rates are extracted from the results of direct numerical simulations plotted versus the scaled channel half-width along with their counterparts calculated by the theory, see Fig. 25b. Quantitatively, the theory predicts higher acceleration rates than numerical simulations. This is because, the numerical simulation does not account for the DL instability, thereby resulting in some moderation of flame acceleration. Qualitatively, numerical results showed that increased in the channel half-width did not cause an increase in the acceleration rate coefficient of the flame.

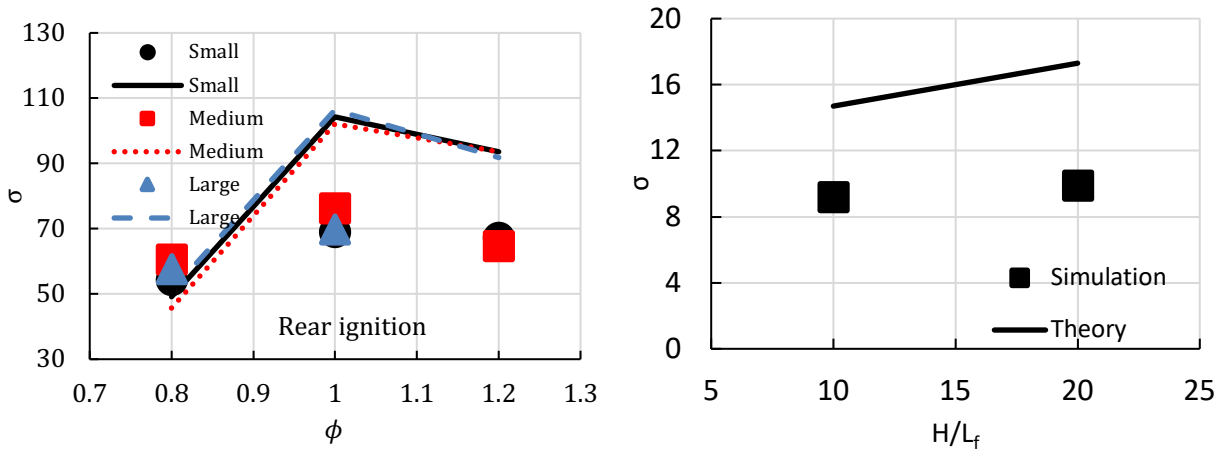


Fig. 25: (a) Comparison of the acceleration rate σ from the experiments (markers) and that calculated from the theory (solid lines) for rear-ignited lean, stoichiometric and rich CH_4 -air explosions in a single cylinder with height of $H = 19$ cm and length of $L = 60$ cm. (b) Comparison of σ from the simulations (markers) and that from the theory (solid lines) for rear-ignited CH_4 -air explosions in a channel with various heights.

4.5 Accomplishments

- An experimental setup has been designed, tested and utilized at WPI. Experimental measurements have been performed and analyzed at this novel experimental platform established at WPI. The measurements have been compared with the computational and theoretical results. Starting from a one-compartment cylindrical vented enclosure, the cylinder was subsequently extended twice in length, and then it was subsequently converted into a two-compartment vessel, with two vents.
- The computational platform entitled “Explosion Vent Analyzer” (EVA) has been further developed and upgraded to methane-air explosions (as well as other blended fuels) in the vented enclosures. Unlike comprehensive CFD modelling, the EVA is simple to learn and use, and it is cheap in terms of the computational time and resources. The EVA is validated to successfully fit the experiments.
- A revised analytical predictive coalmining fire scenario accounting for the wall-attached obstacles has been developed, extended and validated at WVU. Starting initially with gaseous environments, the analysis was subsequently extended to gaseous-dusty environments. Moreover, starting with an incompressible theory, the formulation was subsequently extended to include gas compression.

- Through his work on this project, Dr. Furkan Kodakoglu has successfully graduated from WVU with a PhD degree. The outcome of the project is therefore his PhD dissertation

5.0 PUBLICATION RECORD AND DISSEMINATION EFFORTS

- **Five (5) refereed journal publications**

- ✓ S. Demir, H. Sezer, T. Bush, V. Akkerman, *Promotion & mitigation of premixed flame propagation in a gaseous-dusty environment with various dust distributions*, Fire Safety J. 105 (2019) 270.
- ✓ F. Kodakoglu, H.F. Farahani, A.S. Rangwala, V. Akkerman, *Dynamics of explosion venting in a compartment with methane-air mixtures*, J. Loss Prev. Proc. Ind. 67 (2020) 104230.
- ✓ F. Kodakoglu, S. Demir, D. Valiev, V. Akkerman, *Analysis of gaseous and gaseous-dusty, premixed flame propagation in obstructed passages with tightly placed obstacles*, Fluids 5 (2020) 115.
- ✓ F. Kodakoglu, V. Akkerman, *Analytical study of an effect of gas compressibility on a burning accident in an obstructed passage*, Phys. Fluids 32 (2020) 073602.
- ✓ S. Ogunfuye, H. Sezer, F. Kodakoglu, H.F. Farahani, A.S. Rangwala, V. Akkerman, *Dynamics of explosions in cylindrical vented enclosures: Validation of a computational model by experiments*, Fire 4 (2021) 9.

- **Seven (7) International & National conference papers (including one refereed paper)**

- ✓ F. Kodakoglu, S. Demir, D. Valiev, V. Akkerman, *Towards descriptive scenario of a burning accident in an obstructed mining passage: An analytical approach*, Paper #369, 27th Int. Colloquium on the Dynamics of Explosions and Reactive Systems (ICDERS), Beijing, China, July 28 – Aug. 2, 2019.*

* Refereed paper.

- ✓ F. Kodakoglu, V. Akkerman, *Analytical study of a burning accident in an obstructed coalmining passage*, Paper #2D14, 11th National Combustion Meeting, Pasadena, CA, Mar. 24–27, 2019.
- ✓ F. Kodakoglu, V. Akkerman, *Influence of gas compressibility on a burning accident in an obstructed coalmining passage*, 36th Int. Pittsburgh Coal Conference, Pittsburgh, PA, Sep. 3–6, 2019.
- ✓ H. Sezer, S. Ogunfuye, J. Hashempour, V. Akkerman, *Methane-induced explosions in cylindrical vented enclosures*, Paper #1B02, 42nd Technical Meeting of the Combustion Institute's Eastern States Section, Columbia, SC, Mar. 8–11, 2020.
- ✓ F. Kodakoglu, L. Kareem, V. Akkerman, *The effects of obstructions and gas compressibility on a fire scenario in a coalmining passage*, Paper #1B03, 42nd Technical Meeting of the Eastern States Section of the Combustion Institute, Columbia, SC, Mar. 8–11, 2020.
- ✓ S. Ogunfuye, F. Kodakoglu, L. Kareem, V. Akkerman, *Influence of gas compressibility on a burning accident in an obstructed cylindrical coalmining passage*, Paper #57, 37th Int. Pittsburgh Coal Conference, Pittsburgh, PA, Sept. 8–11, 2020 (Virtual).
- ✓ S. Ogunfuye, H. Sezer, V. Akkerman, *Towards explosion vent analyzer – a computational model predicting explosion parameters of fuel blends*, Paper #1B08, 12th National Combustion Meeting, College Station, TX, May 24–26, 2021 (Virtual).

- **Two (2) conference presentations (Abstracts without papers)**

- ✓ F. Kodakoglu, V. Akkerman, *Analytical predictive formulation for a combustion process in an obstructed coalmining tunnel*, 44th AIAA Dayton-Cincinnati Aerospace Sciences Symposium, Dayton, OH, Mar. 5, 2019.

✓ F. Kodakoglu, V. Akkerman, *Towards analytical description of propane-air premixed combustion in gaseous and gaseous-dusty industrial applications*, 94th Annual Meeting of the West Virginia Academy of Science (WVAS), West Liberty, WV, USA, Mar. 30, 2019.

- **One (1) PhD Dissertation**

✓ F. Kodakoglu, *Experimental, Computational & analytical studies towards a predictive scenario for a burning accident*, PhD Dissertation, West Virginia University, Morgantown, WV, July 2020.

6.0 CONCLUSIONS AND IMPACT ASSESSMENT

As a result of this project, we have further upgraded and validated the Dust and Gas Explosion Model – an integrated analytical, computational and experimental platform to be capable of quantifying the mining fire hazards, namely, the probability of spontaneous ignition, the evolution of a flame front, and the likelihood of a deflagration-to-detonation transition if relevant. A core of the computational component is a fully-compressible, finite-volume Navier-Stokes code solving for the hydrodynamics and combustion equations in a homogeneously-gaseous, laminar environment. The solver is robust, and adapted for parallel computations. As for the newly-developed platform, inert and combustible dust is implemented into the solver by means of thermal-chemical parameters of particle-air flames, tabulated as functions of particle type, size and concentration. In particular, the classical *Seshadri* formulation for the laminar premixed particle-cloud flame speed is employed. It is investigated, systematically, how the noncombustible dust distribution in an obstructed mining passage influences the fire evolution, the flame shape and propagation velocity, as well as the acceleration rate. As a separate component of the computational efforts, another mathematical model – the EVA – is further developed and upgraded to analyze vented explosion scenarios. The EVA solves the corresponding governing equations in a one-zone approximation, including the external explosion produced once the vented mixture is ignited by the expanding flame, to calculate the attained overpressures in relation to the domain geometry and burning conditions. The computational research component of the project was closely connected to accompanying analytic and experimental efforts.

As an analytic component of the project, the entire scenario of premixed flame front evolution within an accidental fire is prescribed, quantitatively, with the situation of a methane-air explosion in an *obstructed* mining passage as the primary application. Specifically, the key stages of flame evolution are scrutinized. First, a globally-spherical expansion of a centrally-ignited, embryonic flame occurs, with a possibility of self-similar acceleration caused by the hydrodynamic instability. This stage provides an order of magnitude increase in the flame speed in realistically large mining passages. Second, it is combined with a mechanism of extremely fast flame acceleration associated with delayed burning in the pockets between the obstacles. Overall, we have identified the key characteristics of all stages such as the timing for each stage as well as the flame shapes, propagation velocities, acceleration rates, run-up distance and flame-generated velocity profiles. We have demonstrated that the flame velocity rises by orders of magnitude, which oftentimes may lead to explosion and detonation triggering. Starting with laminar homogeneously-gaseous combustion, the analysis is subsequently extended to dusty-gaseous environments. Both inert and combustible dust particles are considered. For this purpose, the dependences of the thermal-chemical flame parameters, such as the planar flame speed, on the dust properties, such as the dust particles size and concentration, are incorporated into the formulation, in the same manner as in the computational part, using the *Seshadri* formulation.

In summary, an experimental setup has been designed, tested and utilized at WPI. Experimental measurements have been performed and analyzed at this novel experimental platform established at WPI. The measurements have been compared with the computational and theoretical results. Starting from a one-compartment cylindrical vented enclosure, the cylinder was subsequently extended twice in length, and then it was subsequently converted into a two-compartment vessel,

with two vents. The computational platform entitled “Explosion Vent Analyzer” (EVA) has been further developed and upgraded to methane-air explosions (as well as other blended fuels) in the vented enclosures. Unlike comprehensive CFD modelling, the EVA is simple to learn and use, and it is cheap in terms of the computational time and resources. A revised analytical predictive coalmining fire scenario accounting for the wall-attached obstacles has been developed, extended and validated at WVU. Starting initially with gaseous environments, the analysis was subsequently extended to gaseous-dusty environments. Moreover, starting with an incompressible theory, the formulation was subsequently extended to include gas compression.

Finally, the analytical predictive scenario has been compared to the experiments and the numerical simulations – from the literature, as well as in-situ experiments and modelling performed within the frame of this project, with good agreement obtained. Likewise, the present experimental work agrees with the EVA modelling. Consequently, a newly-developed integrated analytical, computational and experimental Gas & Dust Explosion Model has been validated within the range of its applicability.

Practical Usage of the Project Outcomes

Finally, let us discuss the potential practical applicability of the project outcomes. The key component of the present project, ASTI14FO-82, as well as of the previous project, ASTI14-05, is a quantitative predictive scenario of an accidental explosion and subsequent fire evolution, which is summarized by Eq. (3.31) and references and formulas therein. It is recalled that Eq. (3.31) shows the fire flame location as a function of time. Consequently, based on Eq. (3.31), ***it is possible to estimate how the fire would evolve*** for various mining geometries, and various parameters of the combustible mixture such as composition of methane/air/coal dust mixture, its equivalence ratio; the type, concentration and size of the coal dust particles, etc. Some examples of this calculation is shown in the Appendix.

Moreover, ***this knowledgebase may allow suppressing or mitigating explosion or fire*** behavior by controlling these parameters. In particular, it is shown, qualitatively, how reducing equivalence ratio (ratio of the actual fuel/air ratio to the stoichiometric fuel/air ratio) of the combustible gas (say, methane) and/or the size and concentration of the coal dust may allow avoiding an explosion and/or terminating a fire. If a fire is unavoidable, Eq. (3.31) may allow determining the critical parameters at which the flame evolution can be diminished to a controlled “safe-alarm” level. The latter means that such a fire (even unavoidable) would spread slowly enough that personnel would be able to move to safety if provided early enough warning; see the Appendix.

Finally, if such a disaster as a fast fire is unavoidable, ***our analytical formulation allows predicting whether such a fast fire leads to the detonation initiation*** (the so-called deflagration-to-detonation transition; DDT). If the DDT is unavoidable, its time is estimated by (3.24), with the respective flame run-up distance calculation. It is recalled that the flame run-up distance is the distance the flame spreads before the detonation is initiated; if such a length exceeds the size of the mine opening at the explosion location, then the DDT does not occur. Respectively, the measures how to avoid the DDT by monitoring the equivalence ratio and/or dust size and concentration, employing ventilation and other relevant measures if needed, and thereby augmenting the run-up distance to be large enough should be very useful for safety demands, and this is a direct outcome of Eq. (3.24). It should be noted, in this respect, that even beyond its explosive nature, a detonation is an extremely dangerous event in *enclosures* such as tunnels of coalmines and subways. This is because of shock waves, which can easily kill/injure personnel and destroy expensive equipment in the case of unvented pressure abundance. Consequently, fast flame propagation (if unavoidable and still potentially disastrous) is nevertheless a better option as compared to a detonation. As a result, we are pleased to provide a useful tool predicting if a DDT occurs and a measure how to avoid it if ever possible.

While the fire evolution vs time, Eq. (3.31), and the flame run-up time, Eq. (3.24), and the run-up distance are, presumably, the most useful practical outcomes of our analytical formulation, it recalled that other characteristics of fire and explosion such as the flame shapes and velocities, the flame acceleration rates, and the flow velocity profiles have been identified within the frame of the present analytical endeavors; all of them can be of interest and can be utilized in the concomitant studies. Of course, our analytical formulation is not perfect: in fact, Eqs. (3.24) and (3.31) are associated with a so-called “worst case” scenario, while a fire would develop slower in the practical reality. However, this is completely acceptable in terms of the fire safety viewpoint: indeed, it is better if the reality is safer than a “disaster” predicted by Eq. (3.31) or (3.24), providing us with a certain inherent safety factor.

The experimental component of this project has constituted a culmination of numerous explosion tests in various chambers, with high speed, high resolution, color photography used to systematically capture the volumetric flame characteristics vs time as the explosion evolved in a compartment. These characteristics have been tabulated for a number of varied parameters (the equivalence ratio, ignition location, and vent size) in order to scrutinize the mechanisms of flame movement and its corresponding impact of pressure development in a vented enclosure because of the flame instabilities and turbulence due to obstructions. ***The data obtained can be used to improve the existing practices of gaseous and dusty-gaseous explosion venting, which are correlation-based.*** Consequently, a useful database for such correlations is generated.

In spite of this progress, let us nevertheless recall that the details and impact of turbulence, combustion instabilities, and consequent flame acceleration are not always fully captured by such correlations as they depend on the details of an experiment. This is especially true for gaseous-dusty explosions, the information of which is limited, with the correlations used in commercial codes being questionable. This justifies ***the practical applicability of*** another key goal and outcome of the present project: supplementing the experiments by a ***dual*** computational platform involving (i) the developed and validated *Explosion Vent Analyzer (EVA)* – an *engineering based* explosion venting model for gas and dust explosions in a compartment and (ii) the developed and validated *Gas Explosion Model (GEM)* and *Dusty-Gas Explosion Model (D-GEM)* – the more sophisticated numerical solver(s) based on the computational fluid dynamics (CFD) techniques. As a result, ***the EVA is available for practical usage by any interested user***; this solver is easy to use, fast to pick-up and fast to run. The general version of the EVA has been posted online at the WPI website, while other versions are also available upon request. Unlike the EVA, the GEM/D-GEM package(s) are not so easy to handle. However, the GEM/D-GEM simulations on the subject have been published in the open literature (see, for instance, Ref. [15]), in the form of dimensionless parameters. Consequently, these publications can be used a reference frame for validation of the concomitant and future experimental, computational and analytical works on this subject.

Finally, it is recalled that the WPI experiments were small-scale ones, so this can be used as a reference frame for a future research: extension to an experimental facility of larger scale can be recommended.

Moreover, only gaseous combustion experiments have been performed at the WPI facility within the frame of this project. In the future, it will be expected to extend the WPI experiments to dusty-gaseous combustion, for wider validation.

7.0 RECOMMENDATIONS FOR FUTURE WORK

- Only gaseous combustion experiments have been performed at the WPI facility within the frame of this project. In the future, it will be expected to extend the WPI experiments to dusty-gaseous combustion, for wider validation.
- In addition, the WPI experiments were small-scale experiments, so extension to an experimental facility of larger scale can be recommended as a future work.
- While the Seshadri formulation [2] has been successfully incorporated both in the analytical formulation and the GEM/D-GEM computational platform, thereby fruitfully extending them from the gaseous to gaseous-dusty environments, this has not been done with the EVA as of now. Consequently, it would be great to incorporate the Seshadri formulation into the EVA as well. This would make all present endeavors self-consistent and will open wide possibilities of simple (but viable) simulations of multi-phase explosions.
- In addition, extra work can be recommended on further development of the present integrated experimental-analytical-computational Dust and Gas Explosion Model at larger scales, congested volumes, and multi-compartment enclosures. In fact, the two-compartment experiments and EVA modelling performed in this project was a fragmentary, pilot study, while a systematic work on explosions in multi-compartment vessels will be of great interest – as it may open a possibility for new mining/fire safety measures.

8.0 APPENDIX

We now consider few examples how to employ the analytical predictions in the practical reality. The essence of the formulation is summarized below

$$Z_{tip,o} = \frac{\Theta(1-\alpha)R}{(2\Theta-1)} \left\{ \left[\frac{2\Theta-1}{\Theta-(\Theta-1)(1-\alpha)^2} + 1 \right] \exp \left[\frac{(2\Theta-1)U_{DL}(t_{obs})}{(1-\alpha)R} (t-t_{obs}) \right] - 1 \right\}, \quad (A1)$$

$$\frac{dZ_{tip,0}}{dt} = U_{tip,o} = \Theta U_{DL}(t_{obs}) \left\{ \frac{2\Theta-1}{\Theta-(\Theta-1)(1-\alpha)^2} + 1 \right\} \exp \left[\frac{(2\Theta-1)U_{DL}(t_{obs})}{(1-\alpha)R} (t-t_{obs}) \right]. \quad (A2)$$

$$t_{rud} = t_{obs} + \frac{(1-\alpha)R}{(2\Theta-1)U_{DL}(t_{obs})} \ln \left[\frac{c_0}{\Theta U_{DL}(t_{obs}) \left(\frac{2\Theta-1}{\Theta-(\Theta-1)(1-\alpha)^2} + 1 \right)} \right], \quad (A3)$$

and substituting t_{rud} of Eq. (A3) into Eq. (A1), the flame run-up distance, Z_{rud} , can be found as

$$Z_{rud} = \frac{\Theta(1-\alpha)R}{(2\Theta-1)} \left\{ \left[\frac{2\Theta-1}{\Theta-(\Theta-1)(1-\alpha)^2} + 1 \right] \exp \left[\frac{(2\Theta-1)U_{DL}(t_{obs})}{(1-\alpha)R} (t_{rud}-t_{obs}) \right] - 1 \right\}. \quad (A4)$$

It is recalled that Θ here is the thermal expansion ratio, tabulated for various equivalence ratios ϕ in the literature, and α is the blockage ratio. In particular, an approximate time of a detonation initiation for the $\phi = 0.8$ flame was predicted as $t_{rud} \sim 0.1172$ s for $\alpha = 1/3$ and $t_{rud} \sim 0.0986$ s for $\alpha = 1/2$. Overall, among all equivalence ratios considered, fastest flame acceleration was observed for a slightly fuel-rich flame of $\phi \sim 1.1$. Now, in the case of no obstacles ($\alpha = 0$) and rectangular passages, (luckily!) DDT is not expected at all: the flame skirt contacted the sidewall and stopped acceleration before the DDT event for all ϕ considered. In contrast, it would happen in the presence of obstacles, and the fastest DDT (the shortest run-up distance) occurred for a slightly fuel-rich methane-air

mixture of $\phi \sim 1.1$, with $Z_{rud} \sim 7.34$ m, 6.68 m, 5.37 m for $\alpha = 1/3, 1/2, 2/3$, respectively. For a lean or rich mixture, the run-up distances were much higher: up to ~ 80 m for $\phi = 0.6$ and up to ~ 35 m for $\phi = 1.4$. **As a result, if the characteristic size of a mining passage exceeds Z_{rud} , for a given ϕ we should worry about a possibility of DDT, while otherwise we are on a safe side in terms of DDT.**

In a cylindrical passage, the situation is more disastrous as DDT may happen even in an unobstructed passage ($\alpha = 0$). Here, again, the shortest run-up distances are expected for a slightly fuel-rich methane-air mixture of $\phi \sim 1.1$ as well, with $Z_{rud} \sim 5.47$ m, 4.11 m, 3.45 m, 2.64 m for $\alpha = 0, 1/3, 1/2, 2/3$, respectively. For the lean or rich mixtures, the run-up distances were much higher: up to ~ 40 m for $\phi = 0.6$ and up to ~ 18 m for $\phi = 1.4$. In the case of $\alpha = 0$, the DDT occurred for the equivalence ratios in the range $0.8 \leq \phi \leq 1.3$; while in a leaner or richer mixture a flame skirt contacted the sidewall and a flame started decelerating agreeing with the findings. Once again, **if the characteristic size of a mining passage exceeds Z_{rud} (for a given ϕ) we should worry about a possibility of DDT; otherwise, we are on a safe side in terms of DDT.** In an unobstructed cylindrical passage, we are on a safe side, in terms of DDT, for $\phi < 0.8$ and $\phi > 1.3$. Finally, it is recalled here that the “worst case scenario” is considered, while the practical values of Z_{rud} are lower.

9.0 REFERENCES

1. O.J. Ugarte, V. Bychkov, J. Sadek, D. Valiev, V. Akkerman, *Critical role of blockage ratio for flame acceleration in channels with tightly spaced obstacles*, Phys. Fluids 28 (2016) 093602.
2. K. Seshadri, A. Berlad, V. Tangirala, *Structure of premixed particle-cloud flames*, Combust. Flame 89 (1992) 333.
3. O.J. Ugarte, V. Akkerman, A.S. Rangwala, *A computational platform for gas explosion venting*, Process. Saf. Environ. Prot. 99 (2016) 167.
4. H. Sezer, F. Kronz, V. Akkerman, A.S. Rangwala, *Methane-induced explosions in vented enclosures*, J. Loss Prev. Process. Ind. 48 (2017) 199.
5. https://www.researchgate.net/publication/308982625_Cantera_An_Object-oriented_Software_Toolkit_for_Chemical_Kinetics_Thermodynamics_and_Transport_Processes_Version_220.
6. S. Mulpuru, G.A. Wilkin, *A model for vented deflagration of hydrogen in a volume*. Atomic Energy of Canada Ltd.: Chalk River, Ontario, Canada, 1982.
7. Computer program for calculation of complex chemical equilibrium compositions & applications, I. Analysis <https://www.grc.nasa.gov/www/CEAWeb/RP-1311.htm>.
8. R. Stone, A. Clarke, P. Beckwith, *Correlations for the laminar-burning velocity of methane/diluent/air mixtures obtained in free-fall experiments*, Combust. Flame 114 (1998) 546.
9. S. Liao, D. Jiang, Q. Cheng, *Determination of laminar burning velocities for natural gas*. Fuel 83 (2004) 1247.
10. P. Strakey, *Oxy-combustion fundamentals for direct fired cycles*, National Energy Technology Laboratory (NETL), Pittsburgh, PA, 2017.
11. R. Le Dortz, M. Bellenoue, L. Bonneau, *Laminar burning velocities and Markstein lengths of jet fuel surrogate/air mixtures in a spherical chamber*. 8th European Combustion Meeting, Dubrovnik, Croatia, April, 18–21, 2017.
12. R.J. Kee, M.E. Coltrin, P. Glarborg, H. Zhu, *Chemically reacting flow*; Wiley: Hoboken, NJ, 2017.
13. One-dimensional Flames, Cantera. <https://cantera.org/science/flames.html#kee2017>
14. D.M. Smooke, J.A. Miller, R.J. Kee, *Determination of adiabatic flame speeds by boundary value methods*. Combust. Sci. Technol. 34 (1983) 79.
15. S. Demir, H. Sezer, T. Bush, V. Akkerman, *Promotion & mitigation of premixed flame propagation in a gaseous-dusty environment with various dust distributions*, Fire Safety J. 105 (2019) 270.

16. V. Bychkov, D. Valiev, L.-E. Eriksson, *Physical mechanism of ultrafast flame acceleration*, Phys. Rev. Lett. 101 (2008) 164501.
17. S. Demir, V. Bychkov, S.H.R. Chalagalla, V. Akkerman, *Towards a predictive scenario of a burning accident in a mining passage*, Combust. Theory Modell. 21 (2017) 997.
18. V. Bychkov, V. Akkerman, G. Fru, A. Petchenko, L.-E. Eriksson, *Flame acceleration at the early stages of burning in tubes*, Combust. Flame 150 (2007) 263.
19. V. Akkerman, C.K. Law, V. Bychkov, *Self-similar accelerative propagation of expanding wrinkled flames and explosion triggering*, Phys. Rev. E. 83 (2011) 026305.
20. S. Davis, J. Quinard, G. Searby, *Markstein numbers in counterflow, methane- and propane-air flames: a computational study*, Combust. Flame 130 (2002) 123.
21. F. Kodakoglu, H.F. Farahani, A.S. Rangwala, V. Akkerman, *Dynamics of explosion venting in a compartment with methane-air mixtures*, J. Loss Prev. Proc. Ind. 67 (2020) 104230.
22. B. Fan, X. Jiang, Z. Chen, J. Ye, G. Dong, *Investigation on external explosions during venting*, Fire Saf. Sci. 8 (2005) 1365.
23. D.M. Smooke, J.A. Miller, R.J. Kee, *Determination of adiabatic flame speeds by the boundary value methods*, Combust. Sci. Technol. 34 (1983) 79.
24. S. Ogunfuye, H. Sezer, F. Kodakoglu, H.F. Farahani, A.S. Rangwala, V. Akkerman, *Dynamics of explosions in cylindrical vented enclosures: Validation of a computational model by experiments*, Fire 4 (2021) 9.
25. S. Ogunfuye, F. Kodakoglu, L. Kareem, V. Akkerman, *Influence of gas compressibility on a burning accident in an obstructed cylindrical coalmining passage*, Paper #57, 37th Int. Pittsburgh Coal Conference, Pittsburgh, PA, Sept. 8–11, 2020 (Virtual).
26. S. Ogunfuye, H. Sezer, V. Akkerman, *Towards explosion vent analyzer – a computational model predicting explosion parameters of fuel blends*, Paper #1B08, 12th National Combustion Meeting, College Station, TX, May 24–26, 2021 (Virtual).
27. H. Sezer, S. Ogunfuye, J. Hashempour, V. Akkerman, *Methane-induced explosions in cylindrical vented enclosures*, Paper #1B02, 42nd Technical Meeting of the Combustion Institute's Eastern States Section, Columbia, SC, Mar. 8–11, 2020.
28. F. Kodakoglu, S. Demir, D. Valiev, V. Akkerman, *Analysis of gaseous and gaseous-dusty, premixed flame propagation in obstructed passages with tightly placed obstacles*, Fluids 5 (2020) 115.
29. F. Kodakoglu, S. Demir, D. Valiev, V. Akkerman, *Towards descriptive scenario of a burning accident in an obstructed mining passage: An analytical approach*, Paper #369, 27th Int. Colloquium on the Dynamics of Explosions and Reactive Systems (ICDERS), Beijing, China, July 28 – Aug. 2, 2019.
30. F. Kodakoglu, V. Akkerman, *Analytical study of a burning accident in an obstructed coalmining passage*, Paper #2D14, 11th National Combustion Meeting, Pasadena, CA, Mar. 24–27, 2019.
31. F. Kodakoglu, V. Akkerman, *Analytical predictive formulation for a combustion process in an obstructed coalmining tunnel*, 44th AIAA Dayton-Cincinnati Aerospace Sciences Symposium, Dayton, OH, Mar. 5, 2019.
32. F. Kodakoglu, V. Akkerman, *Towards analytical description of propane-air premixed combustion in gaseous and gaseous-dusty industrial applications*, 94th Annual Meeting of the West Virginia Academy of Science (WVAS), West Liberty, WV, USA, Mar. 30, 2019.
33. M. Kuznetsov, G. Ciccarelli, S.V. Dorofeev, V. Alekseev, Yu. Yankin, T.H. Kim, *DDT in methane-air mixtures*, Shock Waves 12 (2002) 215.
34. E.S. Oran, *Numerical tools for mitigation of methane explosions in coal mines*. Alpha Foundation for the Improvement of Mine Safety & Health, Project AFC215-20, Final Technical Report (2017).
35. F. Kodakoglu, V. Akkerman, *Analytical study of an effect of gas compressibility on a burning accident in an obstructed passage*, Phys. Fluids 32 (2020) 073602.
36. F. Kodakoglu, L. Kareem, V. Akkerman, *The effects of obstructions and gas compressibility on a fire scenario in a coalmining passage*, Paper #1B03, 42nd Technical Meeting of the Eastern States Section of the Combustion Institute, Columbia, SC, Mar. 8–11, 2020.
37. S. Ogunfuye, F. Kodakoglu, L. Kareem, V. Akkerman, *Influence of gas compressibility on a burning accident in an obstructed cylindrical coalmining passage*, Paper #57, 37th Int. Pittsburgh Coal Conference, Pittsburgh, PA, Sept. 8–11, 2020 (Virtual).

